

Review

Metal-Organic Cages Based on Phosphorescent Organometallics

Yunliang Yu ^{1,2,3}, Xiaoxia Wang ¹, Yuliang Liu ^{2,*} and Chao Zou ^{2,*} 

¹ School of Materials Science and Engineering, Dongguan University of Technology, Dongguan 523808, China; yun.liang.yu@hotmail.com (Y.Y.); wangxx@dgut.edu.cn (X.W.)

² Functional Coordination Material Group, Frontier Research Center, Songshan Lake Materials Laboratory, Dongguan 523808, China

³ School of Chemistry and Materials Science, University of Science and Technology of China, Hefei 230026, China

* Correspondence: liuyuliang@sslslab.org.cn (Y.L.); zouchao@sslslab.org.cn (C.Z.)

Abstract: During the last two decades, metal-organic cages (MOCs) have been extensively investigated and well documented. Meanwhile, phosphorescent MOCs have emerged as a kind of new MOC material but have not been given much attention. The diversity of their structures and their flexibility of self-assembly result in various luminescent behaviors. Additionally, their special photoactive properties are quite attractive in the background of photochemistry and worthy of discussion. Here, we would like to introduce the recent development of phosphorescent MOCs, including their structures, syntheses, photophysical properties and possible applications. This minireview may hopefully inspire the development of novel phosphorescent MOCs and also facilitate promising applications.

Keywords: metal-organic cages; phosphorescence; organometallics

1. Introduction

Porous materials, such as metal-organic frameworks (MOFs), have drawn extensive attention in the last few decades [1,2]. In addition, metal-organic cages (MOCs) or metal-organic polyhedrons (MOPs) have also aroused the growing interest of chemists as they have a similar structure to MOFs along with discrete self-assembly, well-defined shapes, extensive porosity and a superior solubility to that of MOFs [3–8]. Since the pioneering work of modern MOCs reported by Saalfrank in 1988 [9], a number of efforts have been devoted to the library of MOCs by Stang [10], Fujita [11], Raymond [12], Cotton [13], Cook [14], Mirkin [15], Hosono and Kitagawa [16], Nitschke [17] and others. A variety of excellent works about these delicate cages have emerged in rapid succession since 2008 (Figure 1, blue column). Among these cages, photoactive cages have recently become a research focus. The high concentration of chromophores and tunable cavities in luminescent MOCs results in host-guest optoelectronic interactions, which have various potential applications, such as in imaging, nonlinear optics, sensors and photocatalysis [18]. However, works on luminescent MOCs are still sparse (Figure 1, shadow column).

Luminescence usually includes fluorescence and phosphorescence. Fluorescence is produced by the radiative electronic transition from the lower vibrational energy level of an excited singlet (S_1) to the ground state (S_0). Phosphorescence is generated from the excited triplet state (T_1) to the ground state (S_0). According to the mechanism of luminescence in metal-organic porous materials, it commonly results from direct metal-centered emissions (usually examined in lanthanide metals), organic ligand excitation (especially from highly conjugated ligands) and charge transfer, including metal-to-ligand charge transfer (MLCT) and ligand-to-metal charge transfer (LMCT). Moreover, the guest molecules in porous materials can also cause luminescence [19–21].



Citation: Yu, Y.; Wang, X.; Liu, Y.; Zou, C. Metal-Organic Cages Based on Phosphorescent Organometallics. *Inorganics* **2023**, *11*, 436. <https://doi.org/10.3390/inorganics11110436>

Academic Editors: Rainer Winte, Wendy Qingyun Wan and Kai Li

Received: 10 October 2023

Revised: 28 October 2023

Accepted: 30 October 2023

Published: 14 November 2023



Copyright: © 2023 by the authors. Licensee MDPI, Basel, Switzerland. This article is an open access article distributed under the terms and conditions of the Creative Commons Attribution (CC BY) license (<https://creativecommons.org/licenses/by/4.0/>).

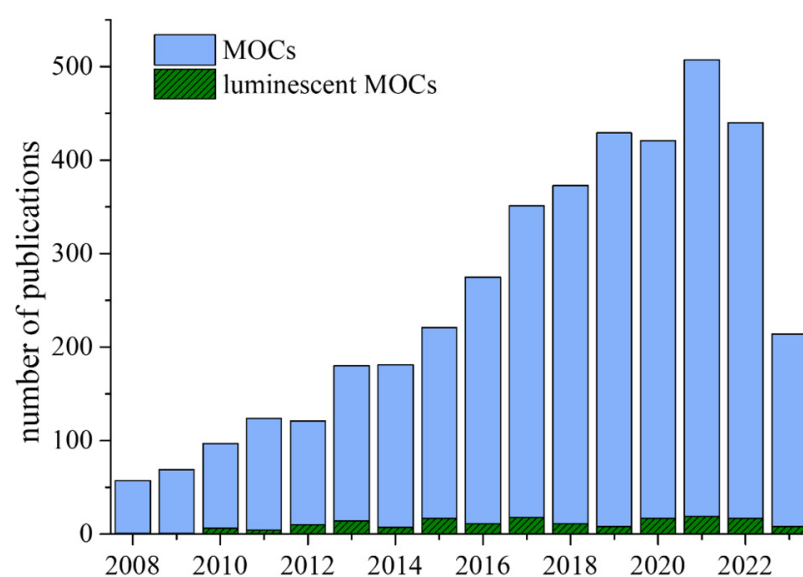


Figure 1. The annual growth of publications in the research of metal-organic cages in Web of Science on the topics of “metal-organic cages” and “luminescent metal-organic cages”, respectively.

Since the rational design and synthesis of MOF materials by researchers, luminescent MOF materials have made great strides. Although people do not often distinguish between the luminescence mechanisms (fluorescence, phosphorescence, etc.) of MOF materials in this field, long-lived luminescent MOF materials (mostly phosphorescence), especially those built with classic ruthenium(II) and iridium(III) metal organic units, combining their adjustable pore structures, have been developed for wide applications in photocatalysis, biological imaging and photodynamic therapy, among other fields [19–21]. MOF materials cannot be dissolved in a solution in a discrete state, which limits their processing and efficient application. However, as porous MOC materials are built by metal organic coordination bonds and their molecularly structured discrete cages can be dissolved in solvents, they hold promise for solving these problems.

Even though luminescent MOC materials are often reported in the literature, the issue of not distinguishing and discussing their luminescence mechanisms (fluorescence, phosphorescence, etc.) still exists. While a number of fluorescent MOCs have been developed by many research groups [22,23], less attention has been paid to the phosphorescence of MOCs. Phosphorescence is widely observed in d-block metal-organic cages, in particular, those containing d^6 , d^8 and d^{10} electronic configurations of second and third-row transition metal ions. These heavy metal atoms not only strengthen spinorbit coupling which could result in efficient intersystem crossing (ISC) from S_1 to T_1 manifolds under photoexcitation, but also relax the spin selection rule which could improve the spin forbidden transition from T_1 to S_0 [24]. Zysman-Colman and his colleagues presented photoactive coordination cages incorporating d-block ruthenium(II) and iridium(III) transition metal complexes in 2018 [18]. In this minireview, we will mainly focus on MOCs derived from phosphorescent organometallic skeletons, especially those incorporating d-block transition metal complexes, and provide an outlook for the basic research and applications of these phosphorescent MOCs. The classification of phosphorescent MOCs mentioned in this minireview is based on the metal type and photophysical properties (Table 1).

Table 1. Summary of phosphorescent MOCs based on the metal type and photophysical properties.

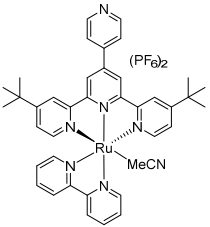
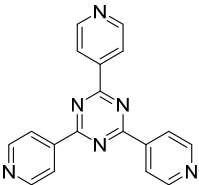
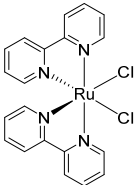
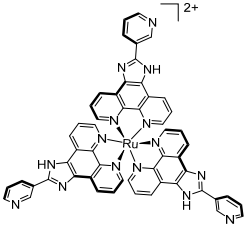
Entry	MOCs	(Metallo) Ligand	Node Precursor	λ_{em} (nm) ^a	Φ_{PL} (%)	τ_{PL} (ns)	Applications
1	MOC-Ru-1 [25] [Ru ₄] (PF ₆) ₆	-	 Ru1	745	1	135	- δ
2	MOC-Ru-2 [26] [L ₄ Ru ₆]Cl ₁₂	 2	 Ru3	577 689 ^b	<0.1	2,790	- δ
3	MOC-Ru-3 [27] [Ru ₈ Pd ₆] (BF ₄) ₂₈	 Ru4	[Pd(MeCN) ₄](BF ₄) ₂	610 ^c	- δ	484	Photocatalysis and bio-imaging

Table 1. Cont.

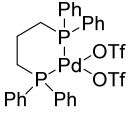
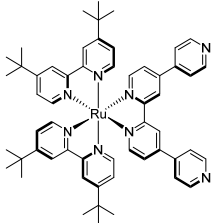
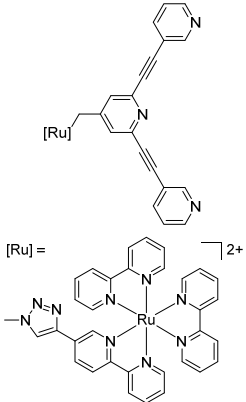
Entry	MOCs	(Metallo) Ligand	Node Precursor	λ_{em} (nm) ^a	Φ_{PL} (%)	τ_{PL} (ns)	Applications
4	MOC-Ru-4a [28] [Ru ₄ Pd ₈] (PF ₆) ₂₄	 <p>Ru5</p>		640	- <i>g</i>	1.21	- <i>g</i>
5	MOC-Ru-5 [29] [Ru ₈ Pd ₄] (BF ₄) ₂₄	 <p>Ru7</p>	[Pd(MeCN) ₄] (BF ₄) ₂	710 ^d	6.9	151 and 700 ^h	- <i>g</i>
6	MOC-Ru-6a [30] [Ru ₄ Pd ₂] (BF ₄) ₁₂	 <p>Ru8</p>	[Pd(MeCN) ₄] (BF ₄) ₂	638 ^e	2.6	659	- <i>g</i>

Table 1. Cont.

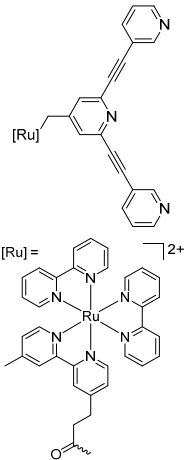
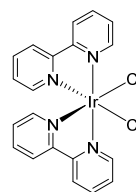
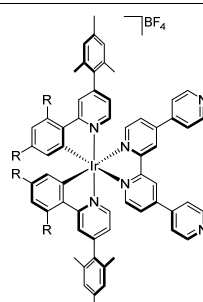
Entry	MOCs	(Metallo) Ligand	Node Precursor	λ_{em} (nm) ^a	Φ_{PL} (%)	τ_{PL} (ns)	Applications
7	MOC-Ru-7b [31] [Ru ₄ Pd ₂] (BF ₄) ₁₂	 <p>Ru11</p>	[Pd(MeCN) ₄] (BF ₄) ₂	640 ^c	66	- ^g	- ^g
8	MOC-Ir-8 [32] [L ₄ Ir ₆] (OTf) ₆	 <p>Ir13</p>		575 ^f	4	- ^g	- ^g
9	MOC-Ir-9 [33] [Ir ₈ Pd ₄] (BF ₄) ₁₆	 <p>Ir14</p>	[Pd(MeCN) ₄](BF ₄) ₂	9a 655, ^d 9b 569 ^d	9a 5, 9b 14	9a 202 9b 825	- ^g

Table 1. Cont.

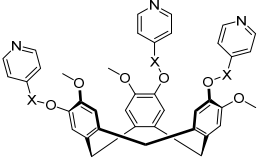
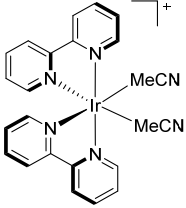
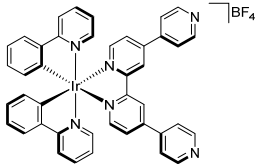
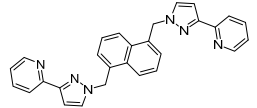
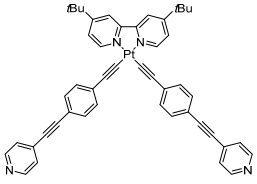
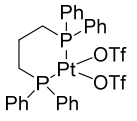
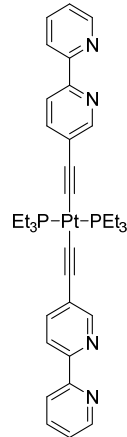
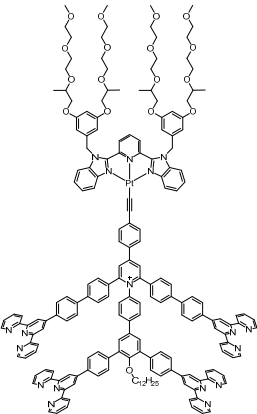
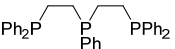
Entry	MOCs	(Metallo) Ligand	Node Precursor	λ_{em} (nm) ^a	Φ_{PL} (%)	τ_{PL} (ns)	Applications
10	MOC-Ir-10 [34] [L ₂ Ir ₃] (PF ₆) ₃	 15	 Ir16	10a 604, ^d 10b 485 ^d	10a 1, 10b 15	10a 59 and 129, ^h 10b 523 and 887 ^h	- ^g
11	MOC-Ir-11 [35] [Ir ₈ Pd ₄] (BF ₄) ₁₆	 Ir17	[Pd(MeCN) ₄](BF ₄) ₂	658 ^c	3.5	141	Bio-imaging and photodynamic therapy
12	MOC-Os-12 [36] [L ₁₂ (Os) ₄ (Cd) ₄] (ClO ₄) ₁₆	 Pt18b	OsCl ₃ ·3H ₂ O Cd(ClO ₄) ₂ ·6H ₂ O	625	2.5	156 and 73 ^h	- ^g
13	MOC-Pt-13b [37] [Pt ₂ Pt ₂] (OTf) ₄	 Pt18b		527	16.7	15,500	- ^g

Table 1. Cont.

Entry	MOCs	(Metallo) Ligand	Node Precursor	λ_{em} (nm) ^a	Φ_{PL} (%)	τ_{PL} (ns)	Applications
14	MOC-Pt-14 [14] [Pt ₆ Zn ₄] (PF ₆) ₈	 Et ₃ P-Pt-PEt ₃ Pt19	Zn(NO ₃) ₂ ·6H ₂ O	545	10	95,000	- ^g
15	MOC-Pt-16 [38] [Pt ₆ Cd ₁₂] (PF ₆) ₃₆	 Pt20	Cd(NO ₃) ₂	567	- ^g	218	- ^g
16	MOC-Au-17 [39] [L ₄ Au ₆ Br] (SbF ₆) ₅	 Ph ₂ P-P-PPh ₂	Chloro(tetrahydrothiophene) gold KBr	485	- ^g	10	- ^g

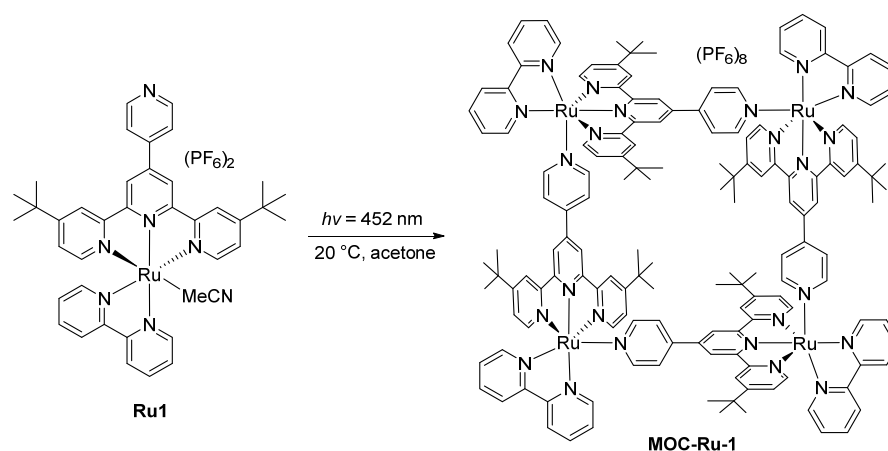
^a In MeCN, at 298 K; ^b at 77 K; ^c in DMSO; ^d in DCM; ^e in DMF; ^f in tetrachloroethane; ^g Not mentioned in the literature; and ^h bi-exponential photoluminescence decay.

2. Metal-Organic Cages Based on Phosphorescent Organometallics

2.1. Phosphorescent MOCs Incorporating d^6 Metal Ion

As important luminophores, phosphorescent transition-metal complexes with a d^6 electronic configuration, especially ruthenium(II) and iridium(III) complexes, whose excited states include metal-to-ligand charge transfer (MLCT), exhibit superior photophysical, thermal and chemical stabilities [40]. Therefore, phosphorescent d^6 transition-metal complexes are usually used for the self-assembly of phosphorescent MOCs.

In 2017, Campagna, Hanan and their colleagues reported a photo-induced luminescent tetraruthenium square, **MOC-Ru-1**, assembled from four terpyridine and four bipyridine ligands with Ru(II) ions as nodes (Scheme 1) [25]. **MOC-Ru-1** possesses the typical $^3\text{MLCT}$ emission of Ru(II) polypyridine complexes at 745 nm with an emission lifetime (τ_{PL}) of 135 ns (40 times greater than that of its mononuclear precursor) and a quantum yield (Φ_{PL}) of 1% in acetonitrile solution at room temperature (Figure 2). This case offers a new route for the assembly of supramolecules via photochemical techniques.



Scheme 1. The luminescent tetraruthenium square **MOC-Ru-1** [25].

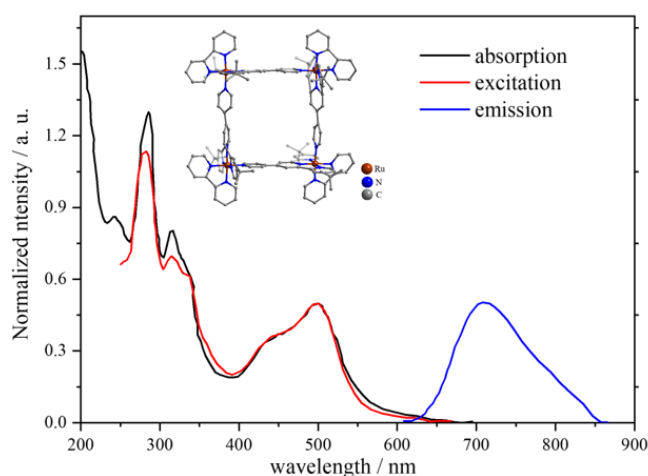
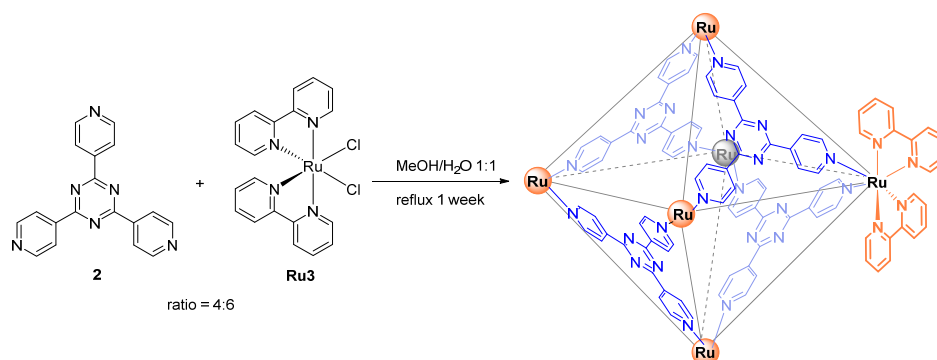


Figure 2. Absorption, excitation and emission spectra of **MOC-Ru-1** in acetonitrile solution at room temperature (adapted from data of [25]).

Another ruthenium(II) cage (**MOC-Ru-2**) with Ru(II) polypyridine complexes as nodes was synthesized by Cook and co-workers through the coordination of 2,4,6-tris(4-pyridyl)-1,3,5-triazine (**TPT**, **2**) with *cis*-bis(2,2'-bipyridine)ruthenium(II) **Ru3** (Scheme 2) [26]. They investigated the photophysical properties of **MOC-Ru-2** in acetonitrile at two different temperatures. The λ_{max} of emissions was 577 nm and 689 nm at room temperature and 77 K, respectively, with a very low Φ_{PL} value of less than 0.1% and biexponential excited

state lifetimes (τ_{PL}) of 2 ns and 790 ns. There is still a red shift of about 0.35 eV (~112 nm) and a biexponential decay in the 77 K emission spectrum compared with those of the room temperature emission, which probably accounted for the existence of two separate but thermally equilibrated triplet excited states, ${}^3\text{ML}(\text{bpy}\pi^*)\text{CT}$ and ${}^3\text{ML}(\text{TPT}\pi^*)\text{CT}$ (Figure 3). The thermal population of this high-energy ${}^3\text{ML}(\text{bpy}\pi^*)\text{CT}$ did not happen at 77 K, and the lower-energy ${}^3\text{ML}(\text{TPT}\pi^*)\text{CT}$ became mainly populated. It is the two separate triplet excited states that give the cage its unique photophysical properties, which encourages the design of new MOCs.



Scheme 2. Coordination-driven self-assembly of the truncated tetrahedral cage **MOC-Ru-2** [26].

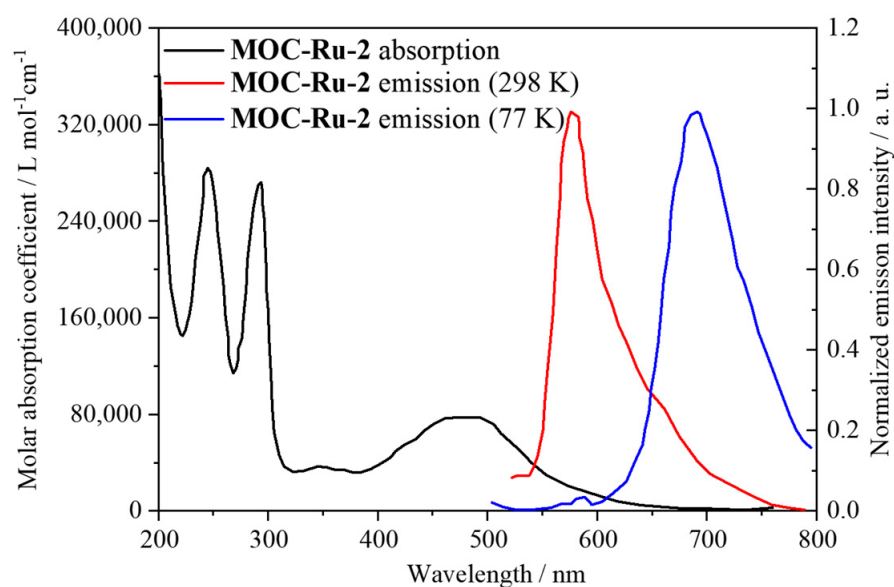
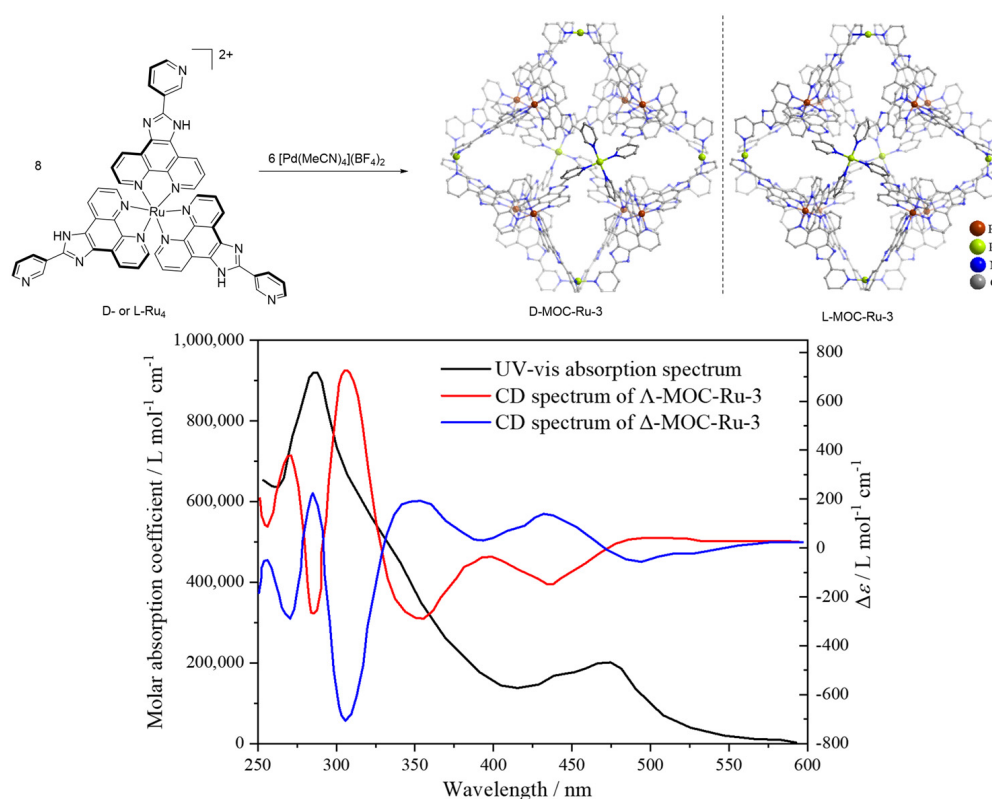


Figure 3. Absorption and emission at 298 K (red; excitation at 430 nm) and 77 K (blue, excitation at 430 nm) of **MOC-Ru-2** in acetonitrile (adapted from data of [26]).

Besides being metal nodes, ruthenium(II) complexes can also be used as ligands for the construction of MOCs. In 2014, Su's group designed and synthesized a nanosized heteronuclear homochiral Pd_6Ru_8 metal-organic cage (**MOC-Ru-3**, Scheme 3) [27,41]. A series of functional and practical applications using this MOC were developed for chiral separation [41], photochemical hydrogen production [42,43], biological imaging [44] and enantioselective photocatalysis [45–47]. The single-crystal X-ray diffraction of this cage exhibited a truncated octahedral, or more accurately, a rhombododecahedron structure with eight metalloligands with **Ru4** comprising the eight faces and six PdN_4 planes truncating the six vertices of the octahedron. The enantiomers Δ - or Λ -**MOC-Ru-3** were generated following four steps. Starting with the chiral induction agent, $\text{K}_2[\text{Sb}_2(+)\text{-tartrate}]_2 \cdot 3\text{H}_2\text{O}$, the racemate $[\text{Ru}(\text{phen})_3]^{2+}$ was first isolated into a pair of enantiomers (Δ - or Λ - $[\text{Ru}(\text{phen})_3]^{2+}$). After oxidizing into Δ - or Λ - $[\text{Ru}(\text{phendione})_3]^{2+}$, Δ - or Λ -**Ru4** metalloligands were ob-

tained from Δ - or Λ [Ru(phenanthroline)₃]²⁺ reacting with 3-pyridinecarboxaldehyde. The final step was the coordination of Δ - or Λ -**Ru4** metalloligands and Pd²⁺ ions to form homochiral Δ - or Λ -**MOC-Ru-3**, respectively. The circular dichroism (CD) spectra of homochiral Δ - or Λ -**MOC-R-3** were measured to monitor their chirality (Scheme 3). Compared with the free **Ru4** metalloligand, **MOC-Ru-3** displayed a similar absorption and emission spectrum in DMSO (Figure 4). The emission maxima at ca. 610 nm stems from Ru(phen)₃-centered triplet ³MLCT states with a τ_{PL} of 601 ns for **Ru4** and 484 ns for **MOC-Ru-3**. A strong π - π^* transition from the intraligand (at 290 nm) in the ultraviolet region and a broad peak corresponding to the metal-to-ligand charge transfer (¹MLCT from Ru to Phen) in the 400–550 nm visible region were observed. The molar absorptivity was intensified at every wavelength, which indicated that the assembly of multiple chromophoric RuL₃ units could form a good light absorber. However, the emission intensity of **MOC-Ru-3** was decreased by ~32% because of the intramolecular charge transfer from RuL₃ to the Pd(pyridine)₄ moieties. In addition, both the DFT calculations and ultrafast transient absorption spectrum demonstrated the electronic structure of **MOC-Ru-3**. At the beginning, the electron was excited from the [Ru(phen)₃]²⁺ chromophore at 400 nm to the ¹MLCT state, then it transferred into the ³MLCT state of the phenanthroline via intersystem crossing (ISC). Followed by the intraligand charge transfer (ILCT) process from phen to biim-py, the excited state relaxation occurred and subsequently arrived to the Pd catalytic center through a much slower process of ligand-to-metal charge transfer (LMCT) (Scheme 4).



Scheme 3. The synthetic route, UV-vis absorption and CD spectra (in H₂O) of homochiral Δ - or Λ -**MOC-Ru-3** (adapted from data of [27,41]).

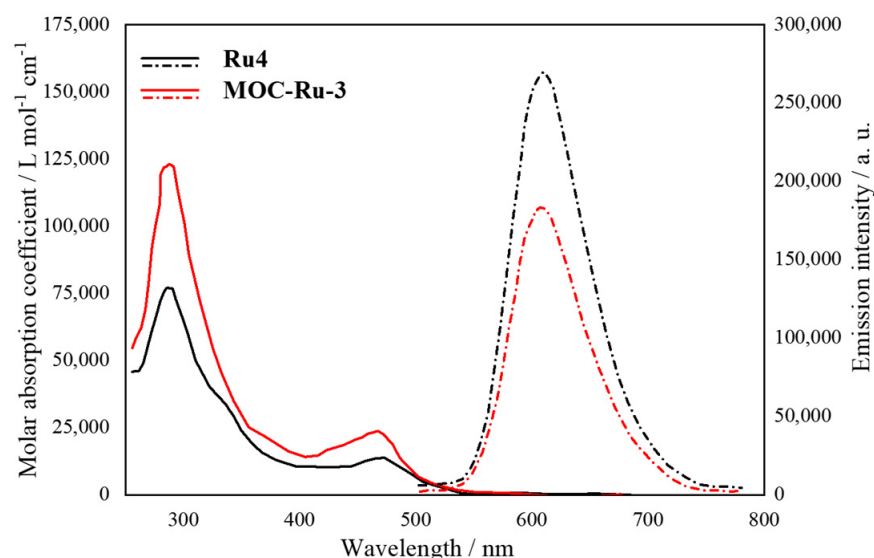
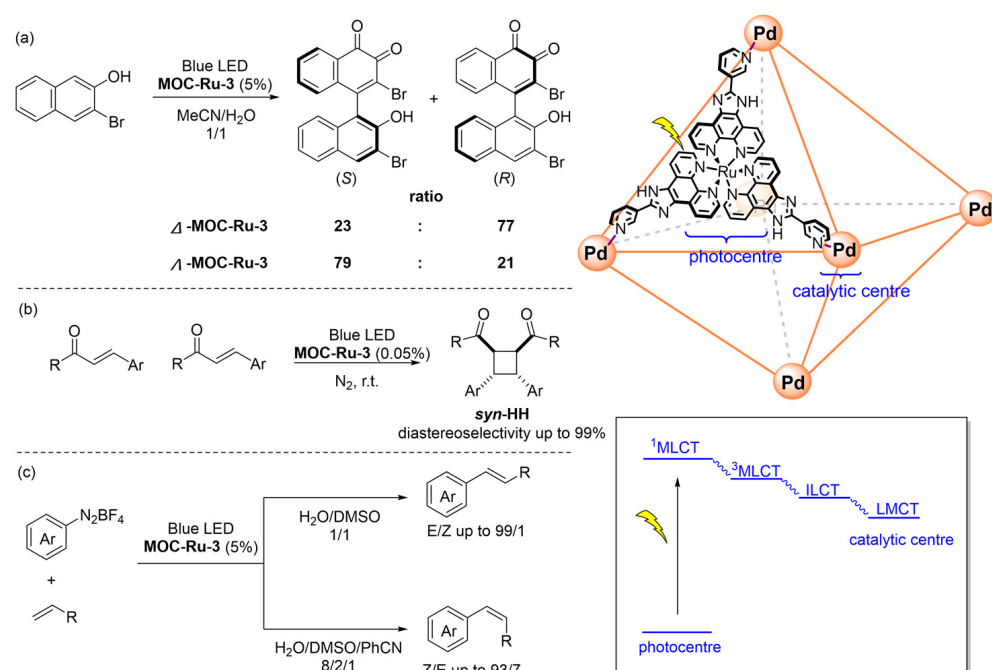


Figure 4. UV-vis absorption and emission spectrum of **Ru4** and 1/8 RuL₃ concentration of **MOC-Ru-3** in DMSO (adapted from data of [42]).

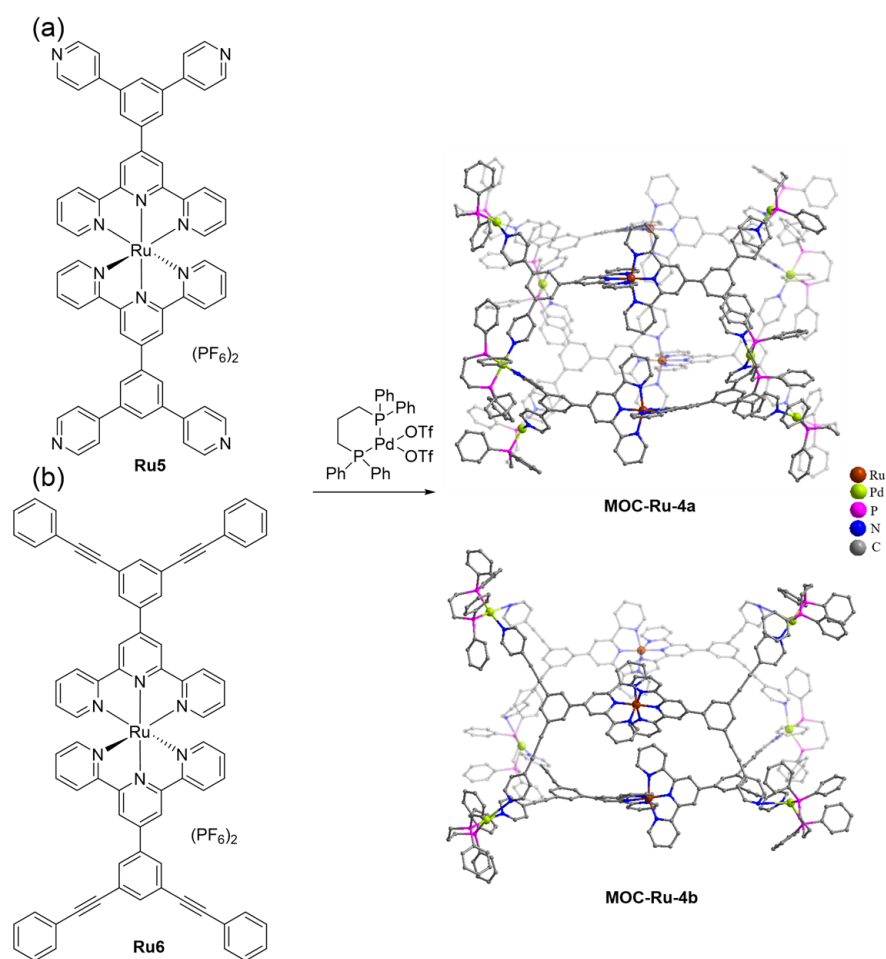


Scheme 4. Photocatalytic reactions: (a) The 1,4-coupling of 3-bromo-2-naphthol in a stereochemical control; (b) the selective intermolecular [2 + 2] cycloaddition; (c) E/Z selective Meerwein arylation, catalyzed by **MOC-Ru-3** with the multi-channel electron transfer routes between Ru and catalytic Pd metal centers [45–47].

Various applications, especially in photocatalysis, have been developed with this multifunctional MOC. The 1,4-coupling of 3-bromo-2-naphthol in a stereochemical control was realized via photoinduction (Scheme 4a) [45]. Under Δ - or Λ -**MOC-Ru-3**, a major *R*- or *S*-1,4'-bis(2-naphthol) product was obtained with both 56% ee, respectively. Another photocatalytic reaction, the selective intermolecular [2 + 2] cycloaddition of α,β -unsaturated carbonyl compounds, was also achieved by **MOC-Ru-3** (Scheme 4b) [46]. This highly efficient and robust cage catalyst could acquire *syn*-HH diastereomers with an excellent diastereoselectivity (up to 99%) and substrate tolerance. Recently, the same group continued to further study photocatalytic reactions with **MOC-Ru-3** and reported the Meerwein

arylation of alkenes with controllable E/Z selectivity using this cage (Scheme 4c) [47]. The desired products were obtained with a high stereoselectivity (E/Z up to 99/1). Moreover, major Z-isomers could be formed through the control of the solvent.

Beves and his colleagues also designed Ru-Pd metal-organic cages (**MOC-Ru-4**) with an inert $[\text{Ru}(\text{tpy})_2]^{2+}$ block (tpy = 2,2',6',2''-terpyridine) decorated with pendant pyridyl rings, which were capable of coordinating to square planar Pd(II) complexes (Scheme 5) [28]. Only a single major species with a tetrameric structure in solution was generated in the reaction of the Ru ligand complex **Ru5** with two equivalents of $\text{Pd}(\text{dppp})(\text{OTf})_2$ (dppp = 1,3-diphenylphosphinopropane) in nitromethane at room temperature (Scheme 5a, **MOC-Ru-4a**). A box-like structure (**MOC-Ru-4a** crystallized in the $P\bar{1}$ space group) with dimensions of ca. $21 \times 21 \times 32 \text{ \AA}$ was observed with Pd(II) centers at each end to construct near-perfect squares (with Pd-Pd-Pd angles of $86.0\text{--}92.8^\circ$ and Pd \cdots Pd distances of $13.2\text{--}13.4 \text{ \AA}$). $[\text{Ru}(\text{tpy})_2]$ units were located at the center of the cage with alternating Ru \cdots Ru distances of 11.82 \AA and 8.78 \AA . The analogous reaction by using the Ru ligand complex **Ru6** obtained a trimeric structure instead of a tetrameric structure (Scheme 5b). These cages have similar photophysical properties with corresponding Ru ligand complexes. The maxima of the $^1\text{MLCT}$ absorption of Ru ligand complexes **Ru5**, **Ru6**, **MOC-Ru-4a** and **MOC-Ru-4b** were at $\lambda_{\text{max}} = 490 \text{ nm}$ (Figure 5a). And the $^3\text{MLCT}$ emission spectra were weak at 640 nm with short mono-exponential excited state lifetimes of $1.26 \pm 0.01 \text{ ns}$ and $1.21 \pm 0.01 \text{ ns}$, respectively (Figure 5b).



Scheme 5. Self-assembly of (a) **MOC-Ru-4a** and (b) **MOC-Ru-4b** [28].

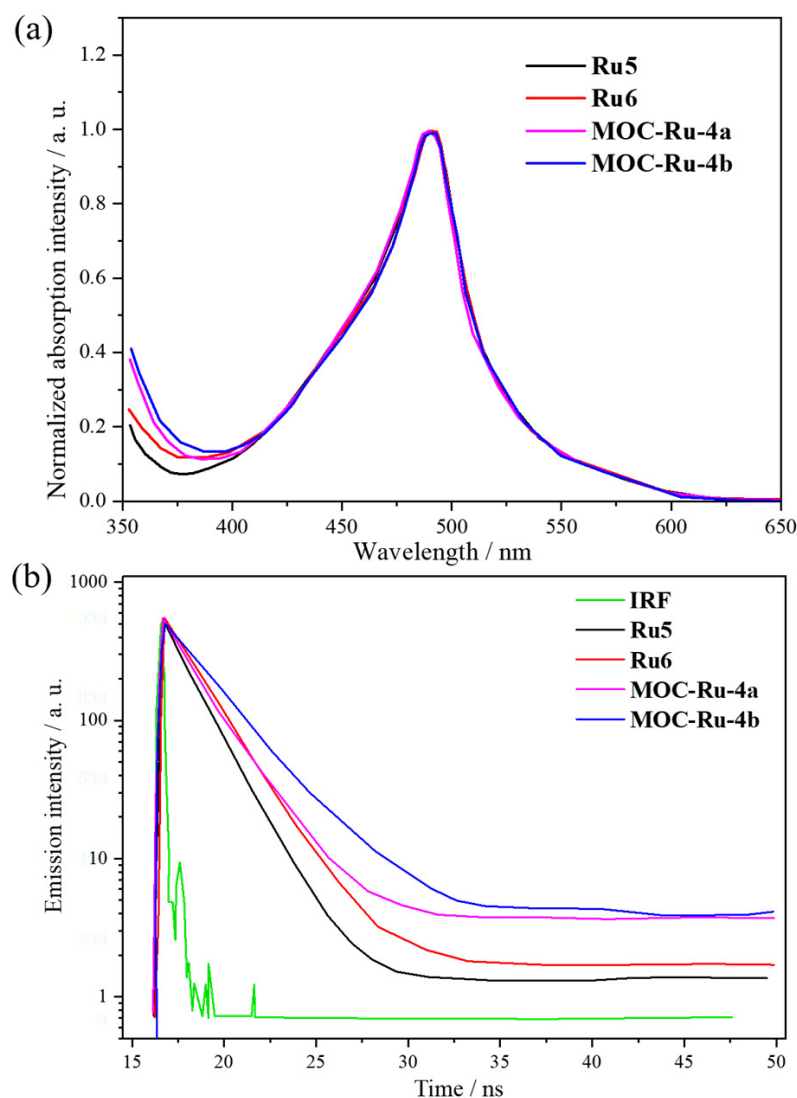
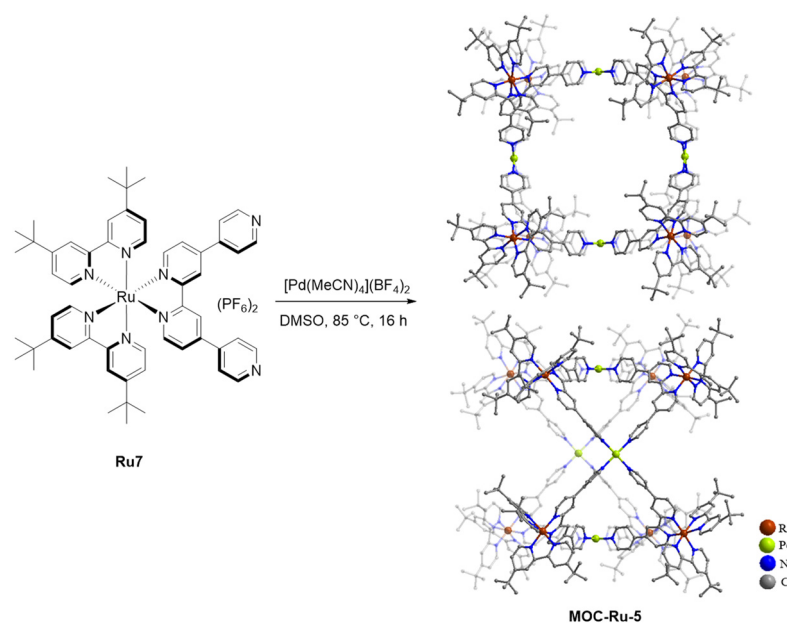


Figure 5. (a) Absorption spectra of **Ru5**, **Ru6**, **MOC-Ru-4a** and **4b**; and (b) the $^3\text{MLCT}$ emission lifetime peaks of **Ru5**, **Ru6**, **MOC-Ru-4a** and **4b**, together with Instrument Response Function (IRF) (adapted from data of [28]).

Another phosphorescent Ru-Pd heteronuclear metal-organic cage (**MOC-Ru-5**) was assembled featuring the metalloligand **Ru7** $[\text{Ru}(\text{dtbubpy})_2(\text{qpy})]^{2+}$ (qpy is 4,4':2',2'':4'',4'''-quaterpyridine and dtbubpy is 4,4'-di-tertbutyl-2,2'-bipyridine) and Pd^{2+} ions by Zysman-Colman's group in 2018 [29]. It is a square arrangement with two ligands doubly bridging adjacent Pd(II) centers in a crown-like fashion, disposing of the four palladium ions (Scheme 6). Different from those of Ruqpy ($\lambda_{\text{PL}} = 674 \text{ nm}$, $\Phi_{\text{PL}} = 7.3\%$), the emission properties of **MOC-Ru-5** in DCM ($\lambda_{\text{PL}} = 710 \text{ nm}$, $\Phi_{\text{PL}} = 6.9\%$) were broader and had a greater red shift owing to the coordination of the Lewis acidic Pd^{II} ions to the ruthenium complex (Figure 6). The π_{qpy}^* orbital level involved in the emission could be stabilized by their coordination, leading to the lower energy of the triplet state. The emission of Ruqpy and **MOC-Ru-5** decayed biexponentially with lifetimes (τ_{PL}) of 324 and 1047 ns, 151 and 700 ns, respectively (Figure 6), which indicated the Pd(II) ions in **MOC-Ru-5** did not adversely affect the photophysical properties of Ru ligand complexes.



Scheme 6. The synthesis and structure of **MOC-Ru-5** viewed down to the crystallographic *a*- (top) and *c*-axes (bottom) [29].

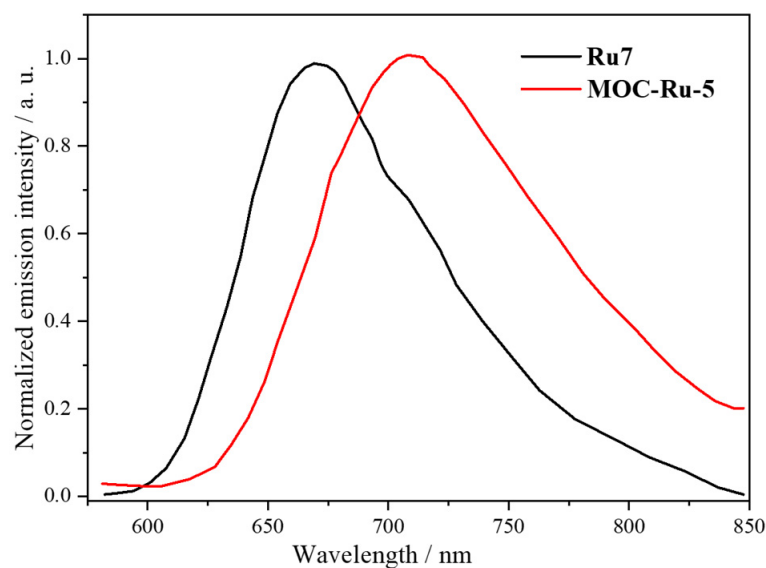
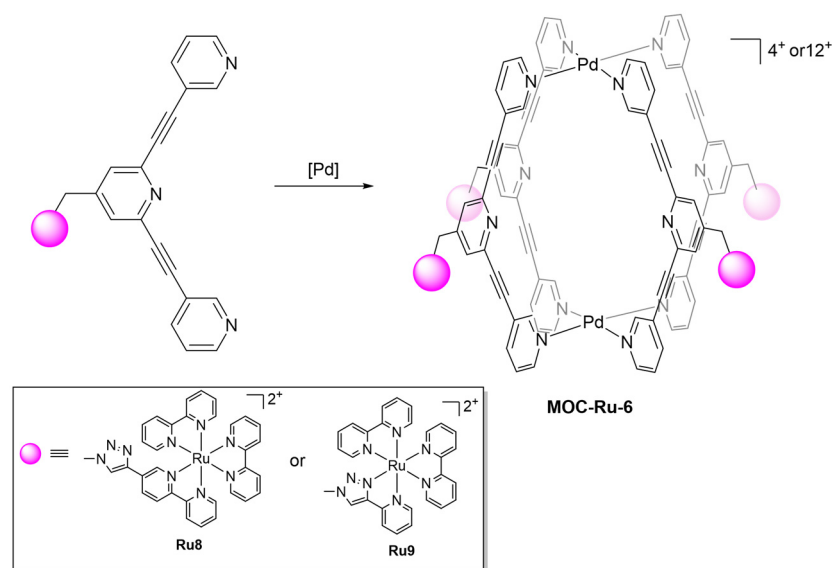


Figure 6. Normalized emission spectra and emission decays of **Ru7** (black line) and **MOC-Ru-5** (red line) in degassed DCM at 298 K (adapted from data of [29]).

Although plenty of Ru-Pd cages have been reported, the emissive nature of these cages is often partially or completely quenched by Pd(II) ions due to non-emissive charge-transfer states between the Ru and Pd centers [18]. Thus, a feasible strategy is to separately append the functionalized units as a pendant ligand at the exohedral [48] or endohedral [49] faces of the assembled cage for electronically isolating the emissive Ru(II) ligand complexes from the Pd(II) ions. In 2016, Crowley, Gordon and their colleagues synthesized $[Pd_2L_4]$ cages with photoactive ruthenium complexes attached at the exohedral face (Scheme 7, **MOC-Ru-6**) [30]. The exo-functionalized ligands were obtained by using the functional tolerant group “click” reaction [50] of copper(I)-catalyzed azide-alkyne cycloaddition (CuAAC). The photophysical properties of **MOC-Ru-6a** and **6b** (ruthenium-based 3MLCT emissions; $\lambda_{PL} = 620$ and 638 nm; $\Phi_{PL} = 0.2\%$ and 2.6% ; $\tau_{PL} = 20$ and 659 ns, respectively) were almost retained with their parent Ru ligand complexes **Ru8** ($\lambda_{PL} = 620$ and 638 nm; $\Phi_{PL} = 0.2\%$ and 6.5% ; $\tau_{PL} = 21$ and 943 ns, respectively) (Figure 7). This strategy offered a practicable

way to keep the functionalization of the parent system in the assembled cages without compromising their photophysical properties.



Scheme 7. Synthesis of $[\text{Pd}_2\text{L}_4]^{4+}$ cages with photoactive ruthenium complexes [30].

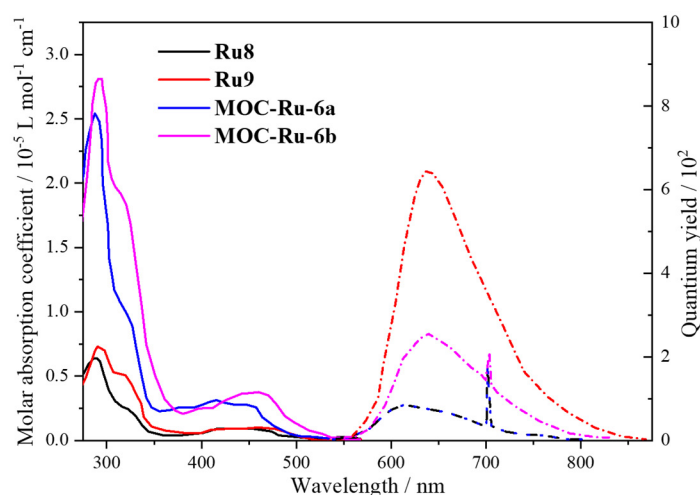
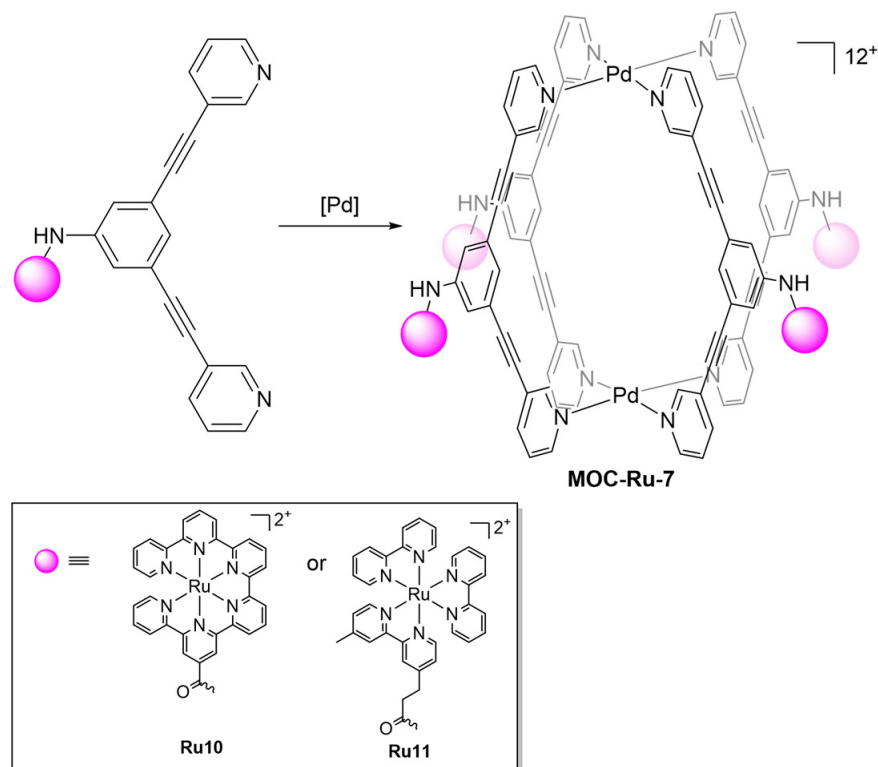


Figure 7. Absorption (solid lines) and emission (dash lines) spectra of **Ru8**, **Ru9**, **MOC-Ru-6a** and **MOC-Ru-6b** (adapted from data of [30]).

Later, analogous exo-functionalized $[\text{Pd}_2\text{L}_4]^{12+}$ cages were demonstrated with Ru(II) pyridine complexes by Casini, Kühn and co-workers (Scheme 8) [31]. The pendant Ru(II) terpyridine and Ru(II) bipyridine moieties were connected by an amide bond to form the ligands **Ru10** and **Ru11**, which mixed with $[\text{Pd}(\text{MeCN})_4](\text{BF}_4)_2$ in DMSO at room temperature, leading to **MOC-Ru-7a** and **7b**. A series of exhaustive spectroscopy analyses were carried out on these cages to study their photophysical properties. The absorption spectra of **MOC-Ru-7** exhibited a range of bands from 250 to 350 nm, which were caused by the strong $\pi\text{-}\pi^*$ transitions of the highly conjugated ligands. Moreover, there is an additional band in the vis region (**MOC-Ru-7a** at 495 nm and **MOC-Ru-7b** at 460 nm) of the UV-vis spectra. The cages displayed interesting emissive properties, which, by varying the molecular structure of the ligand backbone, could increase or decrease the luminescence of the cages. **MOC-Ru-7a** and the corresponding Ru ligand did not show any emissive properties due to the disruption of the chromophoric system in the excited state by the torsion of the amide bond. To avoid bending the amide bond, an alkyl spacer as an

electronic separation was used between the ruthenium moiety and the amide bond of the bis(pyridyl) ligand. Upon irradiation at 260 nm, the Ru ligand **Ru11** and cage **MOC-Ru-7b** emitted strong orange phosphorescence at $\lambda_{\text{PL}} = 640$ nm with unusually high Φ_{PL} values of 88% and 66%, respectively (Figure 8).



Scheme 8. Synthesis of the $[\text{Pd}_2\text{L}_4]^{12+}$ **MOC-Ru-7** [31].

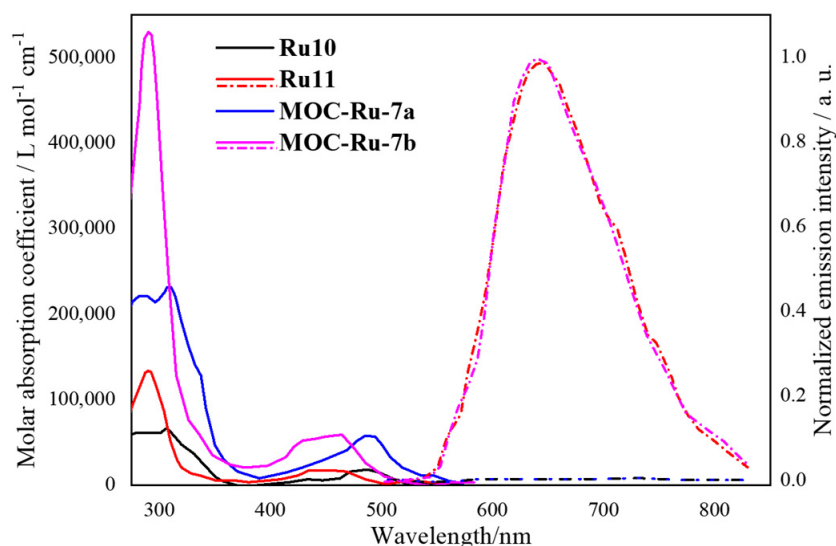


Figure 8. Absorption (solid lines) and emission (dash lines) spectra of **Ru10**, **Ru11**, **MOC-Ru-7a** and **MOC-Ru-7b** (adapted from data of [31]).

Apart from ruthenium(II) complexes, cyclometalated iridium(III) complexes, which also have a d^6 electronic configuration, showed the ability to modulate their emission energy in the visible spectrum and usually were phosphorescent and chemically thermodynamically stable [51]. Therefore, iridium complexes as luminescent moieties have been employed for the assembly of metal-organic cages.

In 2012, the first 3D luminescent and enantiopure Ir(III) octahedral capsule **MOC-Ir-8** ($[(\text{Ir}(\text{ppy})_2)_6(\text{tcb})_4](\text{OTf})_6$ ($\text{tbc} = 1,3,5\text{-tricyanobenzene}$, **12**)) was described by Lusby's group (Figure 9) [32]. Firstly, the enantiomers Λ - and Δ - $[(\text{Ir}(\text{ppy})_2\text{Cl})_2]$ were obtained from resolving *rac*- $[(\text{Ir}(\text{ppy})_2\text{Cl})_2]$ **Ir13** via the chromatographic resolution of *D*- and *L*-serine complexes and their transformation to Λ - and Δ - $[(\text{Ir}(\text{ppy})_2\text{OTf})_2]$ by AgOTf. Then tcb was added into Λ - or Δ - $[(\text{Ir}(\text{ppy})_2\text{OTf})_2]$ to generate corresponding Λ - or Δ -**MOC-Ir-8**, a truncated octahedron with triflates located in each of the octahedron windows. **MOC-Ir-8** emitted orange in a tetrachloroethane (TCE) solution. The emission of Λ - or Δ -**MOC-Ir-8** was broad and there was a red shift at 575 nm with Φ_{PL} values of 4% as compared with those of a reference complex ($[(\text{Ir}(\text{ppy})_2(\text{PhCN})_2)\text{OTf}]$ ($\lambda_{\text{PL}} = 525$ nm, $\Phi_{\text{PL}} < 0.1\%$)) (Figure 10).

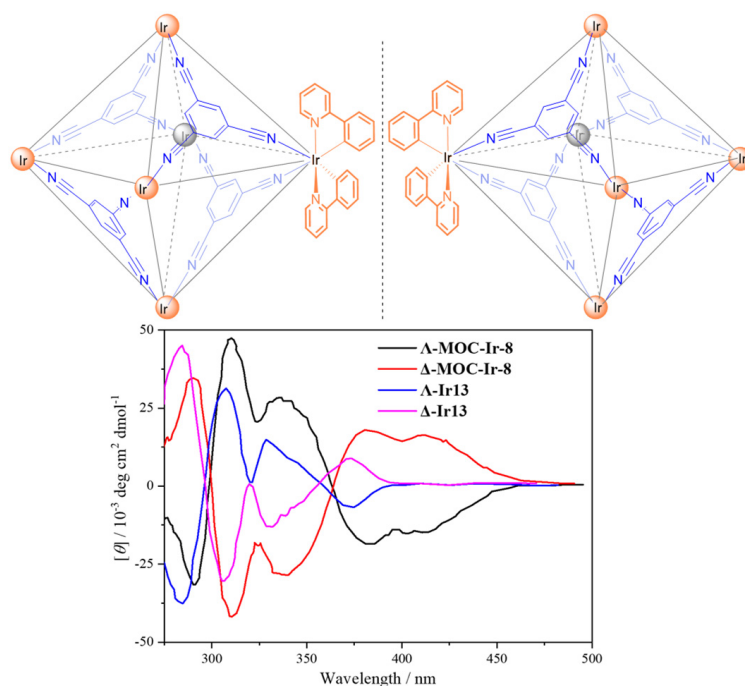


Figure 9. The structure of Λ - and Δ -**MOC-Ir-8** and CD spectra of Λ -**Ir13**, Δ -**Ir13**, Λ -**MOC-Ir-8** and Δ -**MOC-Ir-8** (adapted from data of [32]).

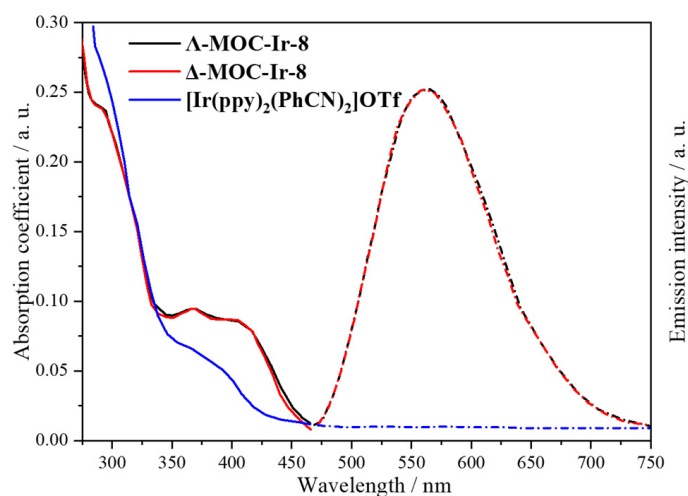
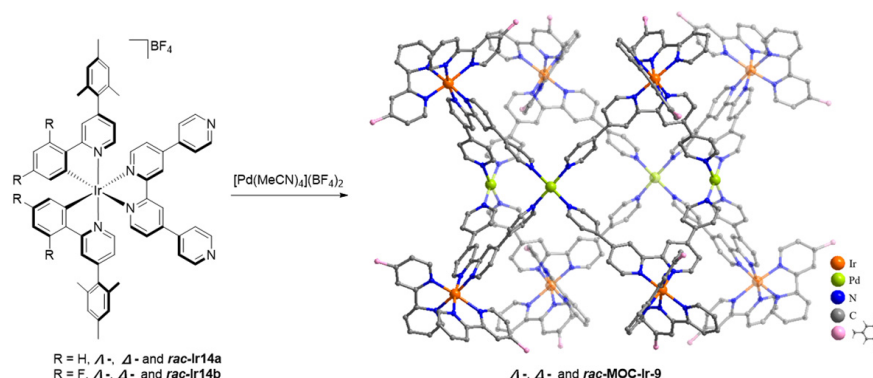


Figure 10. Absorption (solid lines) and emission (dash lines) spectra of $[(\text{Ir}(\text{ppy})_2(\text{PhCN})_2)\text{OTf}]$, Λ - and Δ -**MOC-Ir-8** (adapted from data of [32]).

Subsequently, Zysman-Colman and co-workers revealed the first homochiral red-emitting metal-organic cages $[\text{Ir}_8\text{Pd}_4]^{16+}$, Δ -, Λ - and *rac*-**MOC-Ir-9**, self-assembled by two

enantiopure [52] and racemic Ir(III) ligand complexes, **Ir14** and Pd²⁺ ions (Scheme 9) [33]. The photophysical properties of all enantiomers of the Ir(III) ligand complexes **Ir14** and **MOC-Ir-9** were distinguishable either in DCM solution or in polymethyl methacrylate (PMMA)-doped films. The emission profiles of Δ -, Λ - and *rac*-**MOC-Ir-9a** and Δ -, Λ - and *rac*-**MOC-Ir-9b** had red shifts at 655 nm and 561 nm in degassed DCM, respectively, with lower Φ_{PL} values of 5% and 14%, as well as shorter τ_{PL} values of 202 ns and 825 ns, compared with those of the corresponding Δ -, Λ - and *rac*-**Ir14** ($\lambda_{\text{PL}} = 620$ and 527 nm; $\Phi_{\text{PL}} = 14\%$ and 34%; $\tau_{\text{PL}} = 300$ and 1000 ns, respectively). While in PMMA thin films, the emissions of Δ -**Ir14a**, Δ -**Ir14b**, Δ -, Λ - and *rac*-**MOC-Ir-9a** and Δ -, Λ - and *rac*-**MOC-Ir-9b** had blue shifts at 564 nm, 518 nm, 643 nm and 531 nm, respectively, with higher Φ_{PL} values of 28%, 41%, 10% and 16% and longer multi-exponential τ_{PL} values than those in DCM (Figure 11).



Scheme 9. Self-assembly between the Ir(III) ligands and Pd²⁺ ions for synthesis of **MOC-Ir-9** [33].

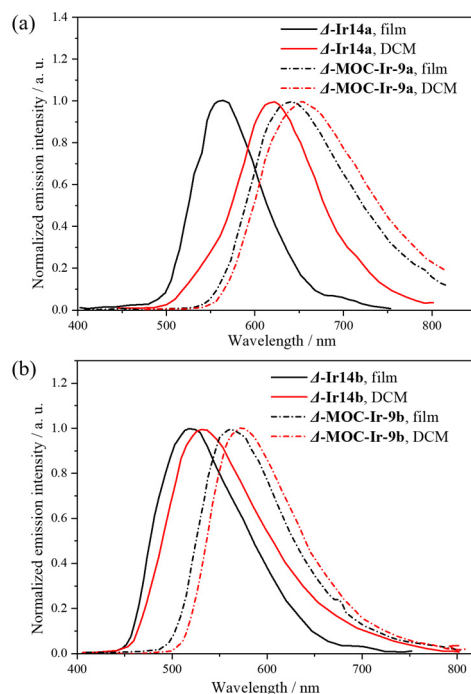
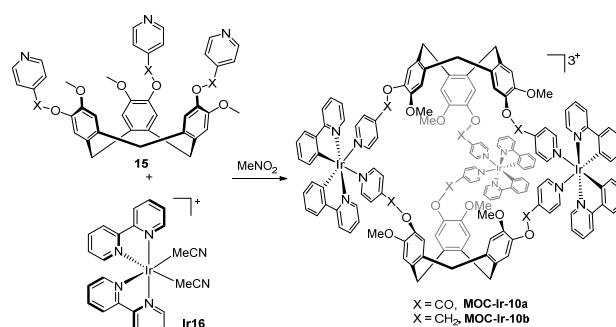


Figure 11. Normalized emission spectra of Ir(III) ligand complexes (a) Δ -**Ir14a**, Δ -**MOC-Ir-9a** and (b) Δ -**Ir14b** and Δ -**MOC-Ir-9b** in deaerated DCM and in PMMA thin films (adapted from data of [33]).

In 2017, Zysman-Colman, Hardie and their colleagues demonstrated that two metal-organic cages, $[(\text{Ir}(\text{ppy})_3)_3(\text{CTV})_2]^{3+}$ **MOC-Ir-10**, could be self-assembled by the chiral tripodal ligands cyclotrimeratrylene (CTV, **15**) and *rac*- $[\text{Ir}(\text{ppy})_2(\text{NCMe})_2]$ **Ir16** (Scheme 10) [34]. **MOC-Ir-10** contained three pseudo-octahedrally coordinated Ir(III) centers, including two

ppy ligands (**Ir16**) and two pyridyl groups from two CTV ligands (**15**) as bridges connecting with the Ir(III) centers in *cis*-arrangements. Notably, homochiral self-sorting could be observed during the process of self-assembly. Although there were 12 potential cage stereoisomers, only two enantiomeric cages (*MM*- $\Lambda\Lambda\Lambda$ and *PP*- $\Delta\Delta\Delta$) were generated with slow self-sorting. The emission properties of **MOC-Ir-10** were examined in DCM solution, as powders and in PMMA-doped films (Figure 12). The **MOC-Ir-10a** powder had a red shift ($\lambda_{\text{PL}} = 648 \text{ nm}$) higher than that in DCM solution ($\lambda_{\text{max}} = 604 \text{ nm}$) with low Φ_{PL} values of around 1% in both media and short bi-exponential emission decays ($\tau_{\text{PL}} = 55$ and 203 ns as a powder; $\tau_{\text{PL}} = 59$ and 129 ns in DCM). Meanwhile, in the film, there was a blue shift at $\Phi_{\text{PL}} = 514 \text{ nm}$ with a higher photoluminescence quantum yield ($\Phi_{\text{PL}} = 5.5\%$) and longer bi-exponential excited state lifetime ($\tau_{\text{PL}} = 634 \text{ ns}$ and 2319 ns) (Figure 12a). For **MOC-Ir-10b**, a vibronic ^3LC emission was more predominant, leading to a greater blue shift emission than that of **MOC-Ir-10a**. Simultaneously, **MOC-Ir-10b** possessed similar energies in DCM, as a powder and in PMMA-doped films at 516 nm with enhanced Φ_{PL} values (15%, 1.6% and 10%, respectively) and bi-exponential τ_{PL} values (523 and 887 ns; 141 and 1175 ns; and 688 and 3042 ns, respectively) (Figure 12b).



Scheme 10. Self-assembly of **MOC-Ir-10** by chiral tripodal ligands and *rac*-[Ir(ppy)₂-(NCMe)₂] [34].

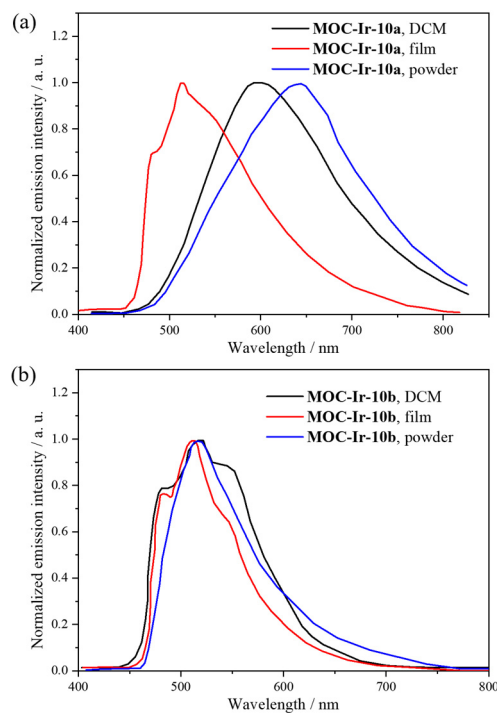
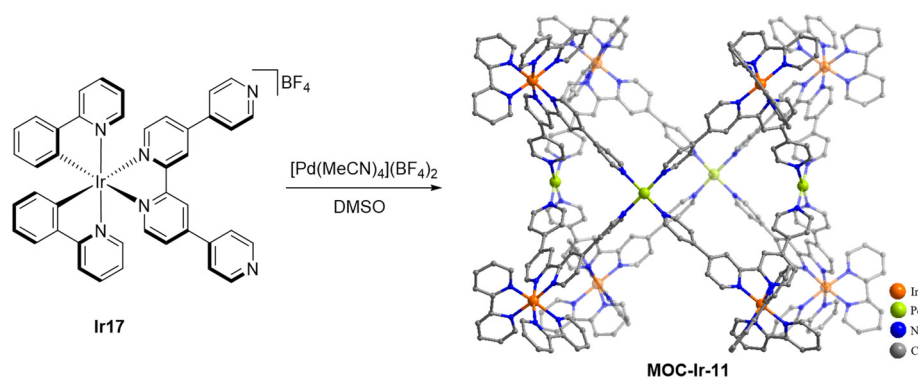


Figure 12. Normalized photoluminescence spectra of (a) **MOC-Ir-10a** and (b) **MOC-Ir-10b** in DCM solution, as powders and in PMMA-doped films (adapted from data of [34]).

The same researchers reported a similar structure, Ir_2L_3 , as above with CTV-type ligands bearing azo-aromatic linkers [53]. Interestingly, the E/Z photoisomerization of the pyridyl-azo-phenyl groups in these cages was observed by photoirradiation with a high-powered laser, and reversible isomerization occurred with blue light. Despite the weak emission of these cages, there was still a deep blue light at ca. 450 nm.

In 2019, Su group presented a heteronuclear Ir_8Pd_4 metal-organic cage, **MOC-Ir-11**, of the form of the bipodal Ir(III) ligand complex $[\text{Ir}(\text{ppy})_2(\text{qpy})(\text{BF}_4)]$ **Ir17** (qpy = 4,4':2',2'':4'',4'''-quaterpyridine; ppy = 2-phenylpyridine) and Pd(II) ions (Scheme 11) [35]. The bipodal Ir(III) ligand complex **Ir17**, bearing two coordinated 2-phenylpyridine units, as well as one coordinated bipyridine linker with two pendants' pyridine (Py), was mixed with $\text{Pd}(\text{CH}_3\text{CN})_4(\text{BF}_4)_2$ at 80 °C to obtain the cubic-barrelled, heteronuclear $\text{Ir}_8\text{-Pd}_4$ **MOC-Ir-11**. The photophysical properties of **MOC-Ir-11** were investigated in the DMSO solution. The photoluminescent excitation and emission spectra of **MOC-Ir-11** were similar compared to those of its corresponding Ir(III) ligand complex **Ir17** with excitation λ_{PL} values of 470 and 430 nm and emission λ_{PL} values of 658 and 654 nm, respectively (Figure 13). Their excited state lifetimes (τ_{PL}) in solution of 141 and 158 ns (**MOC-Ir-11** and Ir(III) ligand complex **Ir17**, respectively) were longer than those in the solid state with quantum yields (Φ_{PL}) of 3.5% and 11%, respectively, at room temperature. Upon visible light irradiation, this cage exhibited one-photon and two-photon excited deep red emissions and a large singlet oxygen quantum yield, which offer possibilities for organelle-targeted cell imaging and photodynamic therapy (PDT).



Scheme 11. Synthesis of **MOC-Ir-11** [35].

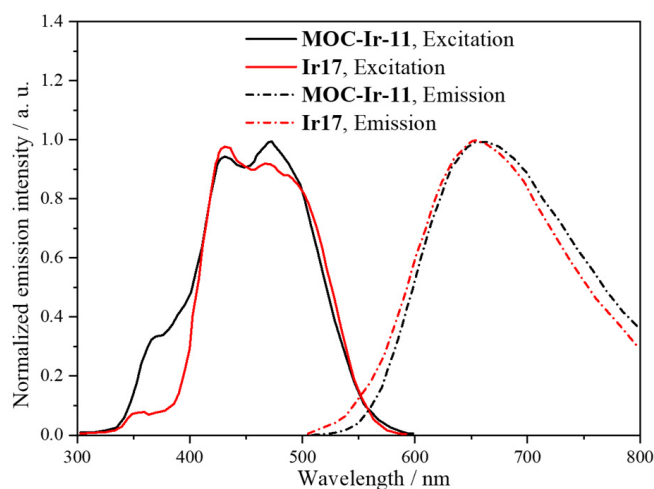
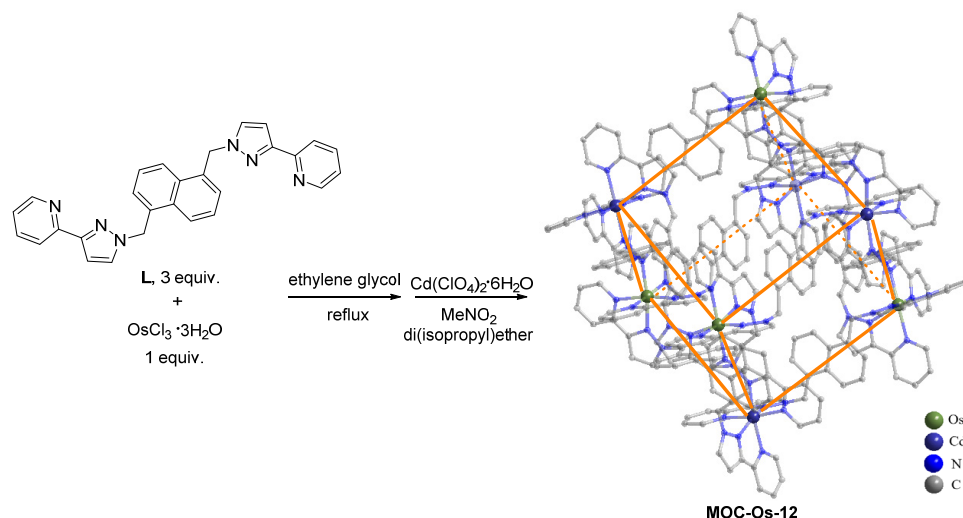


Figure 13. The photoluminescent excitation (solid lines) and emission spectra (dash lines) of **MOC-Ir-11** and Ir(III) ligand complex **Ir17** (adapted from data of [35]).

The d^6 metal ion Os(II) coordinated with ligands in its d-d state possessed a high amount of energy but could not provide a thermally accessible deactivation pathway, leading to the luminescence of the lowest-energy $^3\text{MLCT}$ state. An octanuclear heterometallic

coordination cage $[L_{12}(M^a)_4(M^b)_4]^{16+}$, **MOC-Os-12** was obtained via self-assembly by the pyrazolyl-pyridine ligand **18** with Os(II) and Cd(II) (Scheme 12) [36]. The photophysical properties of **MOC-Os-12** in MeCN had a broad emission at $\lambda_{\max} = 625$ nm with a Φ_{PL} of 2.5% and biexponential lifetimes (τ_{PL}) of 156 ns (minor) and 73 ns (major).



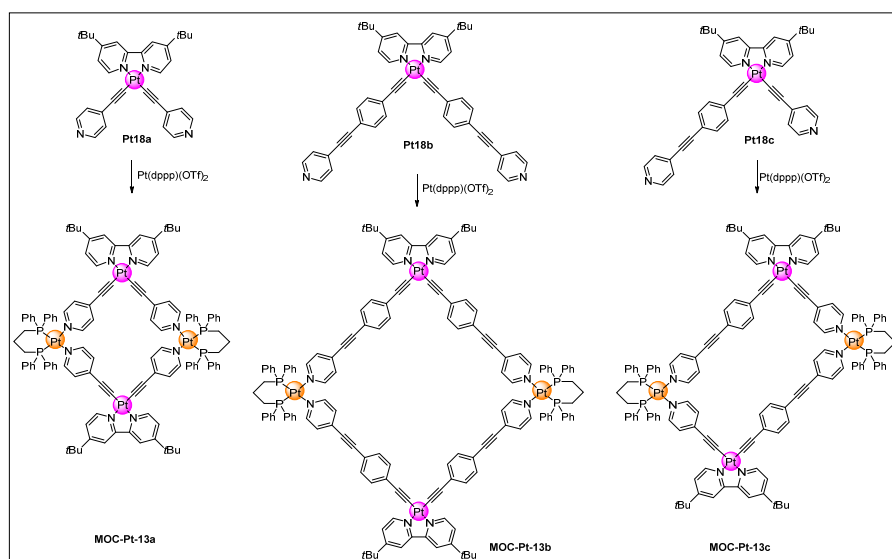
Scheme 12. The synthesis of **MOC-Os-12** (orange line represented octanuclear heterometallic coordination cage) [36].

As d^6 metal-organic complexes naturally have six-coordinate octahedral building blocks, whether as node metals or skeleton components as mentioned previously, it is easier to construct phosphorescent porous structural units based on the principle of symmetrical ligands. In comparison, d^8 and d^{10} metal-organic units adopt square planar and linear coordination modes, with axial open coordination spaces. It is relatively more difficult to establish a structurally stable 3D porous cage while retaining the luminescent properties of phosphorescent metal-organic units without quenching, and there are also fewer reported examples in the literature.

2.2. Phosphorescent MOCs Incorporating d^8 Metal Ion

Due to having planar geometry with an open axial site (defined as the z -axis), d^8 transition-metal complexes are apt to generate dimers (or aggregates) in the ground state or excimers in the excited state via intermolecular metal-metal and ligand-ligand interactions, resulting in metal-metal-to-ligand charge transfer ($^1/3\text{MMLCT}$) excited states [24]. For examples, Pt(II) complexes, because of the presence of $\text{Pt(II)} \cdots \text{Pt(II)}$ interactions, usually display unique photophysical, self-assembly properties as well as conductivity [54,55], which may provide unique pathways for assembling phosphorescent cages.

In 2011, Castellano, Sallé and co-workers synthesized a series of Pt(II) square planar metallocycles (**MOC-Pt-13**) via the self-assembly of bridging pyridine ligands (**Pt18**) containing phenyleneethynylene moieties offering a ligand-localized triplet pathway (intramolecular charge transfer sensitization) for excited-state decay, contributing to their phosphorescence (Scheme 13) [37]. The phosphorescent emissions of **MOC-Pt-13b** and **13c** centered between 524 and 527 nm with Φ_{PL} values of 16.7% and 11.0% as well as τ_{PL} values of 15.5 μs and 17.1 μs , respectively (Figure 14).



Scheme 13. Synthesis of MOC-Pt-13 metallocycles [37].

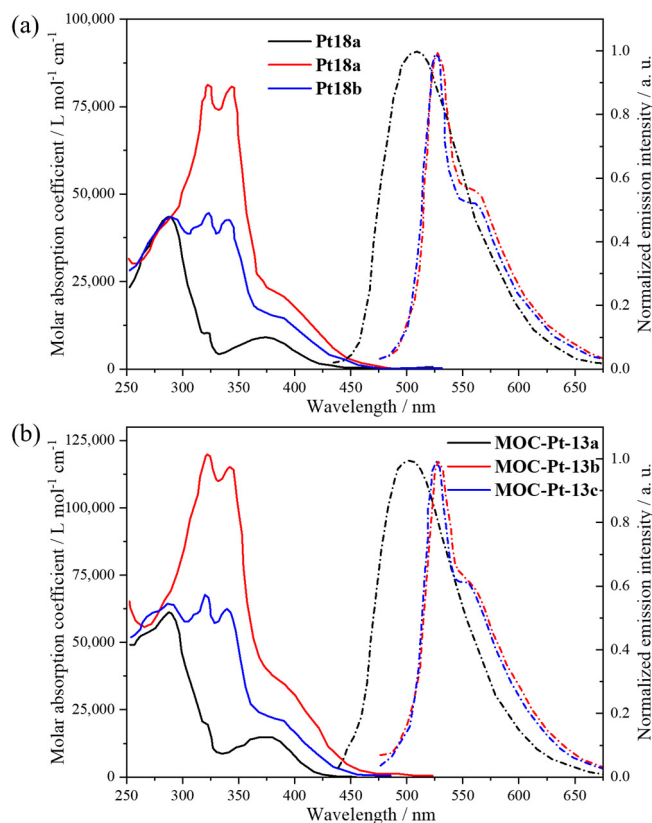
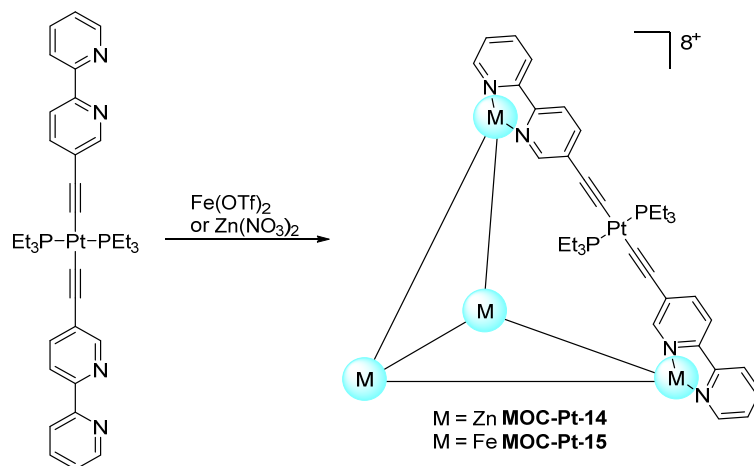


Figure 14. (a) Absorption (solid lines) and emission (dash lines) spectra of Pt18. (b) Absorption (solid lines) and emission (dash lines) spectra of MOC-Pt-13 (adapted from data of [37]).

In 2017, Cook and co-workers reported two phosphorescent tetrahedral cages in the form of bimetallic Pt-Zn, $[\text{Zn}^{\text{II}}_4\text{Pt}_6](\text{PF}_6)_8$ (MOC-Pt-14) and $[\text{Fe}^{\text{II}}_4\text{Pt}_6](\text{OTf})_8$ (MOC-Pt-15), which were coordinated via $\text{Zn}(\text{NO}_3)_2 \cdot 6\text{H}_2\text{O}$ or $\text{Fe}(\text{OTf})_2$ and the linker $\text{Pt}(\text{PE}_3)_2(\text{C}\equiv\text{C-bpy})_2$ Pt19 (Scheme 14) [14]. Four transition-metal nodes as vertices containing bipyridyl ligands from six Pt ligand complexes (Pt19) as edges composed a tetrahedral cage. The molar absorption coefficient of MOC-Pt-15 at $\lambda_{\text{max}} = 402$ nm was significantly higher than that of MOC-Pt-14 and the Pt ligand complex Pt19 ($\lambda_{\text{max}} = 393$ and 360 nm, respectively). The emission spectra of both cages and the Pt ligand complex Pt19 were examined in an N_2 -degassed solution

at 25 °C (Figure 15). All of compounds exhibited very weak fluorescence and differing phosphorescence values. The phosphorescence emission of **MOC-Pt-4** centered at 545 nm with a Φ_{PL} of 10% and τ_{PL} of 95 μs from an $IL\ ^3\pi^*_{\text{C}\equiv\text{C-bpy}} \rightarrow ^1\pi_{\text{C}\equiv\text{C-bpy}}$ transition. Meanwhile, the weak phosphorescence quantum yield of **MOC-Pt-15** was less than 0.1%, probably due to nonradiative competition from emissions from [Fe] nodes, introducing a low-energy $^5\text{M}_{\text{Fe}}\text{C}$ state [56].



Scheme 14. Synthesis of **MOC-Pt-14** and **MOC-Pt-15** [14].

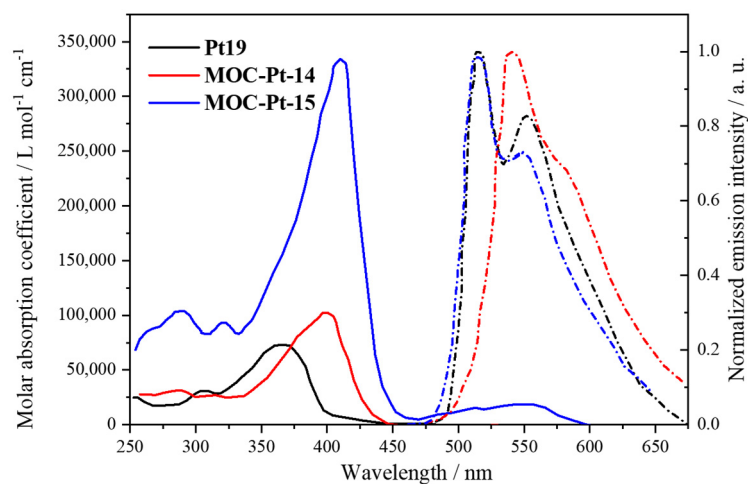
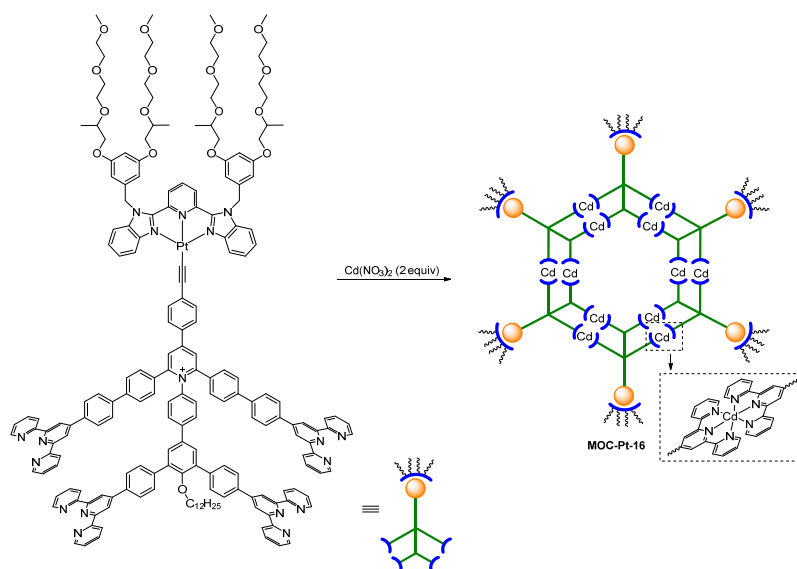


Figure 15. Molar absorption coefficients and normalized phosphorescent emission spectra of **Pt19**, **MOC-Pt-14** and **MOC-Pt-15** (adapted from data of [14]).

The strong intermolecular Pt...Pt interaction [57] among Pt(II) luminophores could promote aggregations and emissions through the aggregation-induced phosphorescent emission (AIPE) effect [58]. In 2020, Li's group devised the giant, discrete metallo-supramolecular concentric hexagon **MOC-Pt-16** via the self-assembly of Pt(II) bzimpy **Pt20** (bzimpy = 2,6-bis(benzimidazole-2'-yl)pyridine) motifs with 2,2':6',2''-terpyridine (tpy) and Cd(II) (Scheme 15) [38]. The Pt(II) bzimpy motif contained four parts, a terminal alkynyl group for installing the Pt(II) motif with a stable and rigid Pt(II)-alkynyl bond to connect the other parts, four tpy arms at the sides for the coordination of Cd(II) to connect the other motifs, multiple hydrophilic ethylene glycol chains on the periphery and a long alkyl chain (C12) into the interior for manipulating the aggregation via balancing the whole hydrophobicity or hydrophilicity. The final metallosupramolecular **MOC-Pt-16** was assembled by six Pt(II) bzimpy motifs and twelve Cd(II), where the size was larger than 10 nm and the molecular weight was beyond 26,000 Da. The emission spectra of the Pt(II) bzimpy motif **Pt20** and **MOC-Pt-16** were similar due to their similar original

emitting excited states in acetonitrile solutions at room temperature (Figure 16). Both of the emission wavelengths were at $\lambda_{PL} = 567$ nm with τ_{PL} values of 270 and 218 ns, respectively. In N_2 -deoxygenated acetonitrile/water solvent ($\lambda_{ex} = 370$ nm), **MOC-Pt-16** displayed a significant improvement in terms of its AIPE compared with that of the Pt(II) bzimpy motif via synergistically combining the AIPE from Pt(II) luminophores and AIE properties from Cd(II)-tpy moieties.



Scheme 15. Synthesis of Pt ligand complex and self-assembly of **MOC-Pt-16** [38].

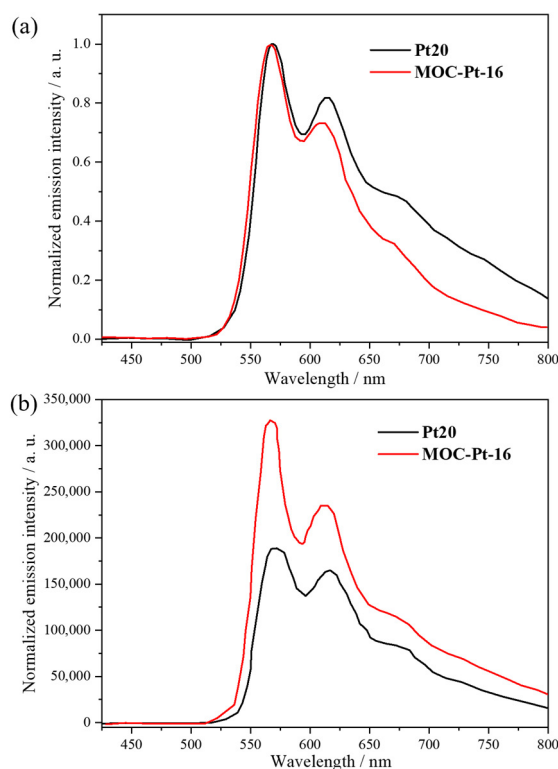


Figure 16. Normalized emission spectra (a) in N_2 -deoxygenated acetonitrile and (b) in N_2 -deoxygenated acetonitrile/water solvent of Pt(II) bzimpy **Pt20** motif and **MOC-Pt-16** (adapted from data of [38]).

2.3. Phosphorescent MOCs Incorporating d^{10} Metal Ion

Complexes of d^{10} transition metals, especially coinage metal complexes such as Cu(I), Ag(I) and as Au(I), either with or without metallophilic interactions, could lead to special spectroscopic properties in the absorption and emission spectra [54,55]. Moreover, the d^{10} - d^{10} metal-metal interactions in gold(I) complexes were stronger and thus were named as “aurophilic” by Schmidbaur [59], always rendering them phosphorescent.

In 2019, Balch’s group demonstrated the mono-bromo box $[\text{Au}_6(\text{Triphos})_4\text{Br}](\text{SbF}_6)_5 \cdot 6(\text{CH}_2\text{Cl}_2)$ **MOC-Au-17** and the dibromo box $[\text{Au}_6(\text{Triphos})_4\text{Br}_2 \cdot \text{H}_2\text{O}](\text{SbF}_6)_4 \cdot 4(\text{CH}_2\text{Cl}_2)$ **MOC-Au-18** by the synthesis of $[\text{Au}_3(\text{Triphos})_2](\text{SbF}_6)_3$ salt in dichloromethane mixed with potassium bromide (the equivalent of one for the mono-bromo box and twice as much for the dibromo box) in methanolic solution [39]. The mono-bromo box **MOC-Au-17** included a bromide ion disordered over two sites and two dichloromethane molecules. The dibromo box **MOC-Au-18** had a similar shape to that of the mono-bromo box. Interestingly, despite there being no aurophilic interactions in these gold boxes because of the dispersion of the Au(I) ion, phosphorescence was produced from the three-coordinate gold(I) complexes [60]. The excitation and emission spectra of **MOC-Au-17** and **MOC-Au-18** were at an excitation λ_{max} of 359 nm and an emission λ_{max} of 485 nm and an excitation λ_{max} of 372 nm and an emission λ_{max} of 496 nm, respectively, with emission lifetimes of 10 μs and 12 μs , respectively, resulting from the phosphorescence (Figure 17).

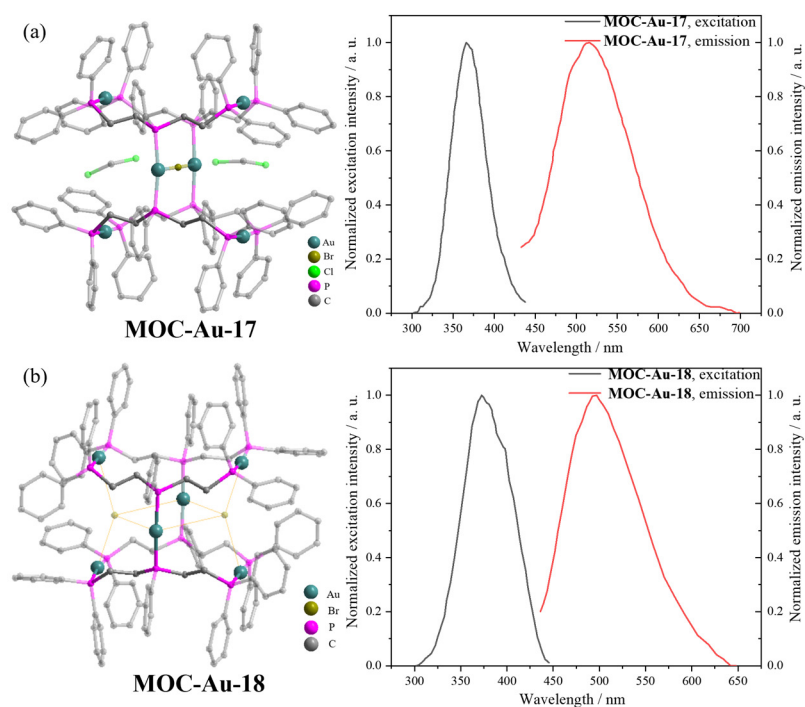


Figure 17. The excitation and emission spectra of (a) **MOC-Au-17** and (b) **MOC-Au-18** (adapted from data of [39]).

Stang’s group reported the host-guest coordination cage had an enhanced absorptivity and prolonged triplet state lifetime [61]. The host-guest coordination cage possessed a broadened visible light absorption range compared with that of the guest molecular coronene and MOC because of the encapsulation-induced core-to-cage charge transfer. Under visible light irradiation, the microenvironment inside the MOC promoted an electrostatic interaction between the light-induced excited electron of the coronene and the positive charge of the node of the MOC. Then the transition-metal node promoted inter-system cross-coupling and attenuated nonradiative decay. These processes provided an enhanced phosphorescence and a prolonged triplet lifetime.

3. Conclusions and Prospect

There is no doubt that phosphorescent metal-organic cages have aroused increasing interest among chemists due to their unique luminescent properties, such as their varied emissive triplet excited states, long lifetimes and large Stokes shift. As multifunctional materials, they have been preliminarily applied in chemical catalysis, biomedicine, sensors, molecular recognition and electro-optical devices. The rapid growth of research on luminescent metal-organic cages in recent decades has established fundamental guiding principles for the design and self-assembly of discrete metal-organic cages. Although considerable efforts have been devoted to the research of luminescent metal-organic cages, it is still at the exploration stage. In this minireview, we have summarized the recent works on phosphorescent MOCs, including their structures, luminescence properties and potential applications, aiming to offer some guidance on their synthesis and a greater understanding of their photochemical/physical features.

However, recently relatively few phosphorescent MOCs have been reported, and their structures and functions are also relatively simple and targetless due to the instability of MOCs resulting from relatively weak and reversible coordination bonds [3]. Thus, in general, efficient and concise assembled strategies need to be fully developed for further exploration. Furthermore, the coordination of phosphorescent ligands and metal nodes result in the quenching of luminescence via nonradiative deactivation, leading to a low-photoluminescence quantum yield, which is also a challenge to be solved. Some organic linkers with high-conjugated π electrons, such as pyrene- and naphthalene-based organic linkers and heterometal-organic ligands with special phosphorescent properties, are expected to be potential candidates for the construction the phosphorescent MOCs. Moreover, the encapsulation of photoactive guests in the cages to excite phosphorescence is also another attractive method.

Considering the unique luminescence properties of phosphorescent MOCs, comprehensive experimental studies will need to focus on screening their phosphorescent properties, such as their wavelength, lifetime and quantum yield, for the establishment of a phosphorescent MOC database. Simultaneously, an in-depth understanding of and studies on the mechanism of phosphorescent MOCs, including the origin of their phosphorescence and the relationship between their structure and luminescence, will contribute to the improvement and optimization of their functions and properties.

Currently, most applications of phosphorescent MOCs are limited to the lab scale, such as those in photocatalysis, biomedicine and optoelectronic materials. The regulation of the relationship between their structure and properties via the suitable choice of components (for phosphorescence, reversible redox activity, etc.) is key, along with the delicate control of pore size. Moreover, host-guest interactions will also offer a novel method for the assembly of MOCs. Recently, there has been significant progress in the development of phosphorescent systems based on first-row transition-metal organic complexes [62]. However, there are no reports on the use of such organometallic skeletons to construct MOC materials. This may also be a future research and exploration direction. Future development will focus on the new synthetic exploration, efficient assembly and specific photoactivity of MOCs. It is anticipated that more and more new phosphorescent MOCs will be available for practical applications following continuing efforts in this field.

Author Contributions: Conceptualization, Y.L. and C.Z.; investigation, Y.Y. and Y.L.; writing—original draft preparation, Y.Y. and Y.L.; writing—review and editing, Y.L., X.W. and C.Z. All authors have read and agreed to the published version of the manuscript.

Funding: Y.Y., Y.L. and C.Z. acknowledge support from the National Natural Science Foundation of China (21901109, 22302136) and Guangdong Basic and Applied Basic Research Foundation (2020A1515011448) as well as start-up funding from Songshan Lake Materials Laboratory (Y1D1061C11).

Data Availability Statement: No new data were created.

Conflicts of Interest: The authors declare that they have no known competing financial interests or personal relationships that could have appeared to influence the work reported in this paper.

References

1. Furukawa, H.; Cordova, K.E.; O’Keeffe, M.; Yaghi, O.M. The chemistry and applications of metal-organic frameworks. *Science* **2013**, *341*, 1230444. [[CrossRef](#)]
2. Gong, W.; Chen, Z.; Dong, J.; Liu, Y.; Cui, Y. Chiral Metal-Organic Frameworks. *Chem. Rev.* **2022**, *122*, 9078–9144. [[CrossRef](#)] [[PubMed](#)]
3. Pan, M.; Wu, K.; Zhang, J.-H.; Su, C.-Y. Chiral metal-organic cages/containers (MOCs): From structural and stereochemical design to applications. *Coord. Chem. Rev.* **2019**, *378*, 333–349. [[CrossRef](#)]
4. El-Sayed, E.M.; Yuan, Y.D.; Zhao, D.; Yuan, D. Zirconium Metal-Organic Cages: Synthesis and Applications. *Acc. Chem. Res.* **2022**, *55*, 1546–1560. [[CrossRef](#)] [[PubMed](#)]
5. Vardhan, H.; Yusubov, M.; Verpoort, F. Self-assembled metal-organic polyhedra: An overview of various applications. *Coord. Chem. Rev.* **2016**, *306*, 171–194. [[CrossRef](#)]
6. Lee, S.; Jeong, H.; Nam, D.; Lah, M.S.; Choe, W. The rise of metal-organic polyhedra. *Chem. Soc. Rev.* **2021**, *50*, 528–555. [[CrossRef](#)]
7. Gosselin, A.J.; Rowland, C.A.; Bloch, E.D. Permanently Microporous Metal-Organic Polyhedra. *Chem. Rev.* **2020**, *120*, 8987–9014. [[CrossRef](#)]
8. Percastegui, E.G.; Ronson, T.K.; Nitschke, J.R. Design and Applications of Water-Soluble Coordination Cages. *Chem. Rev.* **2020**, *120*, 13480–13544. [[CrossRef](#)]
9. Saalfrank, R.W.; Stark, A.; Peters, K.; von Schnering, H.G. The First “Adamantoid” Alkaline Earth Metal Chelate Complex: Synthesis, Structure, and Reactivity. *Angew. Chem. Int. Ed.* **1988**, *27*, 851–853. [[CrossRef](#)]
10. Olenyuk, B.; Whiteford, J.A.; Fechtenkötter, A.; Stang, P.J. Self-assembly of nanoscale cuboctahedra by coordination chemistry. *Nature* **1999**, *398*, 769–799. [[CrossRef](#)]
11. Sun, Q.F.; Iwasa, J.; Ogawa, D.; Ishido, Y.; Sato, S.; Ozeki, T.; Sei, Y.; Yamaguchi, K.; Fujita, M. Self-assembled M₂₄L₄₈ polyhedra and their sharp structural switch upon subtle ligand variation. *Science* **2010**, *328*, 1144–1147. [[CrossRef](#)] [[PubMed](#)]
12. Meyer, M.; Kersting, B.; Powers, R.E.; Raymond, K.N. Rearrangement Reactions in Dinuclear Triple Helicates. *Inorg. Chem.* **1997**, *36*, 5179–5191. [[CrossRef](#)]
13. Cotton, F.A.; Lin, C.; Murillo, C.A. Supramolecular Arrays Based on Dimetal Building Units. *Acc. Chem. Res.* **2001**, *34*, 759–771. [[CrossRef](#)] [[PubMed](#)]
14. Zhang, Y.; Crawley, M.R.; Hauke, C.E.; Friedman, A.E.; Cook, T.R. Phosphorescent Decanuclear Bimetallic Pt(6)M(4) (M = Zn, Fe) Tetrahedral Cages. *Inorg. Chem.* **2017**, *56*, 4258–4262. [[CrossRef](#)]
15. Oliveri, C.G.; Ulmann, P.A.; Wiester, M.J.; Mirkin, C.A. Heteroligated Supramolecular Coordination Complexes Formed via the Halide-Induced Ligand Rearrangement Reaction. *Acc. Chem. Res.* **2008**, *41*, 1618–1629. [[CrossRef](#)]
16. Hosono, N.; Gochomori, M.; Matsuda, R.; Sato, H.; Kitagawa, S. Metal-Organic Polyhedral Core as a Versatile Scaffold for Divergent and Convergent Star polymer Synthesis. *J. Am. Chem. Soc.* **2016**, *138*, 6525–6531. [[CrossRef](#)]
17. Percastegui, E.G.; Mosquera, J.; Ronson, T.K.; Plajer, A.J.; Kieffer, M.; Nitschke, J.R. Waterproof Architectures Through Subcomponent Self-Assembly. *Chem. Sci.* **2019**, *10*, 2006–2018. [[CrossRef](#)]
18. Rota Martir, D.; Zysman-Colman, E. Photoactive supramolecular cages incorporating Ru(II) and Ir(III) metal complexes. *Chem. Commun.* **2018**, *55*, 139–158. [[CrossRef](#)]
19. Gutiérrez, M.; Zhang, Y.; Tan, J.-C. Confinement of Luminescent Guests in Metal-Organic Frameworks: Understanding Pathways from Synthesis and Multimodal Characterization to Potential Applications of LG@MOF Systems. *Chem. Rev.* **2022**, *122*, 10438–10483. [[CrossRef](#)]
20. Li, Y.-L.; Li, A.-J.; Huang, S.-L.; Vittal, J.J.; Yang, G.-Y. Polypyridyl Ru(II) or cyclometalated Ir(III) functionalized architectures for photocatalysis. *Chem. Soc. Rev.* **2023**, *52*, 4725–4754. [[CrossRef](#)]
21. Cui, Y.; Yue, Y.; Qian, G.; Chen, B. Luminescent functional metal-organic frameworks. *Chem. Rev.* **2012**, *112*, 1126–1162. [[CrossRef](#)]
22. Cook, T.R.; Stang, P.J. Recent Developments in the Preparation and Chemistry of Metallacycles and Metallacages via Coordination. *Chem. Rev.* **2015**, *115*, 7001–7045. [[CrossRef](#)]
23. Xu, L.; Wang, Y.X.; Yang, H.B. Recent advances in the construction of fluorescent metallocycles and metallocages via coordination-driven self-assembly. *Dalton Trans.* **2015**, *44*, 867–890. [[CrossRef](#)]
24. To, W.-P.; Wan, Q.; Tong, G.S.M.; Che, C.-M. Recent Advances in Metal Triplet Emitters with d₆, d₈, and d₁₀ Electronic Configurations. *Trends Chem.* **2020**, *2*, 796–812. [[CrossRef](#)]
25. Laramee-Milette, B.; Nastasi, F.; Puntoriero, F.; Campagna, S.; Hanan, G.S. Photo-Induced Assembly of a Luminescent Tetra-ruthenium Square. *Chemistry* **2017**, *23*, 16497–16504. [[CrossRef](#)]
26. Hauke, C.E.; Oldacre, A.N.; Fulong, C.R.P.; Friedman, A.E.; Cook, T.R. Coordination-Driven Self-Assembly of Ruthenium Polypyridyl Nodes Resulting in Emergent Photophysical and Electrochemical Properties. *Inorg. Chem.* **2018**, *57*, 3587–3595. [[CrossRef](#)] [[PubMed](#)]
27. Li, K.; Zhang, L.Y.; Yan, C.; Wei, S.C.; Pan, M.; Zhang, L.; Su, C.Y. Stepwise assembly of Pd(6)(RuL(3))(8) nanoscale rhombododecahedral metal-organic cages via metalloligand strategy for guest trapping and protection. *J. Am. Chem. Soc.* **2014**, *136*, 4456–4459. [[CrossRef](#)]

28. Yang, J.; Bhadbhade, M.; Donald, W.A.; Iranmanesh, H.; Moore, E.G.; Yan, H.; Beves, J.E. Self-assembled supramolecular cages containing ruthenium(II) polypyridyl complexes. *Chem. Commun.* **2015**, *51*, 4465–4468. [[CrossRef](#)] [[PubMed](#)]
29. Rota Martir, D.; Cordes, D.B.; Slawin, A.M.Z.; Escudero, D.; Jacquemin, D.; Warriner, S.L.; Zysman-Colman, E. A luminescent [Pd(4)Ru(8)](24+) supramolecular cage. *Chem. Commun.* **2018**, *54*, 6016–6019. [[CrossRef](#)]
30. Elliott, A.B.; Lewis, J.E.; van der Salm, H.; McAdam, C.J.; Crowley, J.D.; Gordon, K.C. Luminescent Cages: Pendant Emissive Units on [Pd2L4](4+) “Click” Cages. *Inorg. Chem.* **2016**, *55*, 3440–3447. [[CrossRef](#)]
31. Schmidt, A.; Hollering, M.; Han, J.; Casini, A.; Kuhn, F.E. Self-assembly of highly luminescent heteronuclear coordination cages. *Dalton Trans.* **2016**, *45*, 12297–12300. [[CrossRef](#)]
32. Chepelin, O.; Ujma, J.; Wu, X.; Slawin, A.M.; Pitak, M.B.; Coles, S.J.; Michel, J.; Jones, A.C.; Barran, P.E.; Lusby, P.J. Luminescent, enantiopure, phenylatopyridine iridium-based coordination capsules. *J. Am. Chem. Soc.* **2012**, *134*, 19334–19337. [[CrossRef](#)] [[PubMed](#)]
33. Rota Martir, D.; Escudero, D.; Jacquemin, D.; Cordes, D.B.; Slawin, A.M.Z.; Fruchtl, H.A.; Warriner, S.L.; Zysman-Colman, E. Homochiral Emissive Lambda(8) -and Delta(8) -[Ir(8) Pd(4)](16+) Supramolecular Cages. *Chemistry* **2017**, *23*, 14358–14366. [[CrossRef](#)]
34. Pritchard, V.E.; Rota Martir, D.; Oldknow, S.; Kai, S.; Hiraoka, S.; Cookson, N.J.; Zysman-Colman, E.; Hardie, M.J. Homochiral Self-Sorted and Emissive Ir(III) Metallo-Cryptophanes. *Chemistry* **2017**, *23*, 6290–6294. [[CrossRef](#)]
35. Li, C.; Wang, Y.; Lu, Y.; Guo, J.; Zhu, C.; He, H.; Duan, X.; Pan, M.; Su, C.Y. An iridium(III)-palladium(II) metal-organic cage for efficient mitochondria-targeted photodynamic therapy. *Chin. Chem. Lett.* **2020**, *31*, 1183–1187. [[CrossRef](#)]
36. Wragg, A.B.; Metherell, A.J.; Cullen, W.; Ward, M.D. Stepwise assembly of mixed-metal coordination cages containing both kinetically inert and kinetically labile metal ions: Introduction of metal-centred redox and photophysical activity at specific sites. *Dalton Trans.* **2015**, *44*, 17939–17949. [[CrossRef](#)]
37. Goeb, S.; Prusakova, V.; Wang, X.; Vezinat, A.; Salle, M.; Castellano, F.N. Phosphorescent self-assembled Pt(II) tetranuclear metalocycles. *Chem. Commun.* **2011**, *47*, 4397–4399. [[CrossRef](#)]
38. Li, Y.; Huo, G.F.; Liu, B.; Song, B.; Zhang, Y.; Qian, X.; Wang, H.; Yin, G.Q.; Filosa, A.; Sun, W.; et al. Giant Concentric Metallosupramolecule with Aggregation-Induced Phosphorescent Emission. *J. Am. Chem. Soc.* **2020**, *142*, 14638–14648. [[CrossRef](#)] [[PubMed](#)]
39. Walters, D.T.; Powers, X.B.; Olmstead, M.M.; Balch, A.L. The Preparation of Luminescent, Mechanochromic Molecular Containers from Non-Emissive Components: The Box Cations, [Au(6) (Triphos)(4) Br](5+) and [Au(6) (Triphos)(4) Br(2)](4). *Chemistry* **2019**, *25*, 3849–3857. [[CrossRef](#)] [[PubMed](#)]
40. Zhao, Q.; Li, F.; Huang, C. Phosphorescent chemosensors based on heavy-metal complexes. *Chem. Soc. Rev.* **2010**, *39*, 3007–3030. [[CrossRef](#)]
41. Wu, K.; Li, K.; Hou, Y.J.; Pan, M.; Zhang, L.Y.; Chen, L.; Su, C.Y. Homochiral D4-symmetric metal-organic cages from stereogenic Ru(II) metalloligands for effective enantioseparation of atropisomeric molecules. *Nat. Commun.* **2016**, *7*, 10487. [[CrossRef](#)] [[PubMed](#)]
42. Chen, S.; Li, K.; Zhao, F.; Zhang, L.; Pan, M.; Fan, Y.Z.; Guo, J.; Shi, J.; Su, C.Y. A metal-organic cage incorporating multiple light harvesting and catalytic centres for photochemical hydrogen production. *Nat. Commun.* **2016**, *7*, 13169. [[CrossRef](#)] [[PubMed](#)]
43. Wu, K.; Li, K.; Chen, S.; Hou, Y.J.; Lu, Y.L.; Wang, J.S.; Wei, M.J.; Pan, M.; Su, C.Y. The Redox Coupling Effect in a Photocatalytic Ru(II) -Pd(II) Cage with TTF Guest as Electron Relay Mediator for Visible-Light Hydrogen-Evolving Promotion. *Angew. Chem. Int. Ed.* **2020**, *59*, 2639–2643. [[CrossRef](#)]
44. Wang, Y.P.; Wu, K.; Pan, M.; Li, K.; Mo, J.T.; Duan, X.H.; He, H.Z.; Shen, J.; Su, C.Y. One-/Two-Photon Excited Cell Membrane Imaging and Tracking by a Photoactive Nanocage. *ACS Appl. Mater. Interfaces* **2020**, *12*, 35873–35881. [[CrossRef](#)]
45. Guo, J.; Xu, Y.W.; Li, K.; Xiao, L.M.; Chen, S.; Wu, K.; Chen, X.D.; Fan, Y.Z.; Liu, J.M.; Su, C.Y. Regio- and Enantioselective Photodimerization within the Confined Space of a Homochiral Ruthenium/Palladium Heterometallic Coordination Cage. *Angew. Chem. Int. Ed.* **2017**, *56*, 3852–3856. [[CrossRef](#)]
46. Wang, J.S.; Wu, K.; Yin, C.; Li, K.; Huang, Y.; Ruan, J.; Feng, X.; Hu, P.; Su, C.Y. Cage-confined photocatalysis for wide-scope unusually selective [2 + 2] cycloaddition through visible-light triplet sensitization. *Nat. Commun.* **2020**, *11*, 4675. [[CrossRef](#)] [[PubMed](#)]
47. Wang, Y.; Chen, J.; Yang, J.; Jiao, Z.; Su, C.Y. Elaborating E/Z-Geometry of Alkenes via Cage-Confined Arylation Catalysis of Terminal Olefins. *Angew. Chem. Int. Ed.* **2023**, *62*, e202303288. [[CrossRef](#)] [[PubMed](#)]
48. Kikuchi, T.; Sato, S.; Fujita, M. Well-Defined DNA Nanoparticles Templated by Self-Assembled M12L24 Molecular Spheres and Binding of Complementary Oligonucleotides. *J. Am. Chem. Soc.* **2010**, *132*, 15930–15932. [[CrossRef](#)]
49. Murase, T.; Sato, S.; Fujita, M. Nanometer-sized shell molecules that confine endohedral polymerizing units. *Angew. Chem. Int. Ed.* **2007**, *46*, 1083–1085. [[CrossRef](#)]
50. Lewis, J.E.; McAdam, C.J.; Gardiner, M.G.; Crowley, J.D. A facile “click” approach to functionalised metallosupramolecular architectures. *Chem. Commun.* **2013**, *49*, 3398–3400. [[CrossRef](#)]
51. Henwood, A.F.; Zysman-Colman, E. Lessons learned in tuning the optoelectronic properties of phosphorescent iridium(III) complexes. *Chem. Commun.* **2017**, *53*, 807–826. [[CrossRef](#)] [[PubMed](#)]

52. Martir, D.R.; Momblona, C.; Pertegas, A.; Cordes, D.B.; Slawin, A.M.; Bolink, H.J.; Zysman-Colman, E. Chiral Iridium(III) Complexes in Light-Emitting Electrochemical Cells: Exploring the Impact of Stereochemistry on the Photophysical Properties and Device Performances. *ACS. Appl. Mater. Interfaces* **2016**, *8*, 33907–33915. [[CrossRef](#)] [[PubMed](#)]
53. Oldknow, S.; Martir, D.R.; Pritchard, V.E.; Blitz, M.A.; Fishwick, C.W.G.; Zysman-Colman, E.; Hardie, M.J. Structure-switching M(3)L(2) Ir(III) coordination cages with photo-isomerising azo-aromatic linkers. *Chem. Sci.* **2018**, *9*, 8150–8159. [[CrossRef](#)] [[PubMed](#)]
54. Yam, V.W.; Wong, K.M. Luminescent metal complexes of d6, d8 and d10 transition metal centres. *Chem. Commun.* **2011**, *47*, 11579–11592. [[CrossRef](#)]
55. Yam, V.W.; Au, V.K.; Leung, S.Y. Light-Emitting Self-Assembled Materials Based on d(8) and d(10) Transition Metal Complexes. *Chem. Rev.* **2015**, *115*, 7589–7728. [[CrossRef](#)]
56. Liu, Y.; Persson, P.; Sundstrom, V.; Warnmark, K. Fe N-Heterocyclic Carbene Complexes as Promising Photosensitizers. *Acc. Chem. Res.* **2016**, *49*, 1477–1485. [[CrossRef](#)]
57. Yu-Lut Leung, S.; Wing-Wah Yam, V. Hierarchical helices of helices directed by Pt · · Pt and π - π stacking interactions: Reciprocal association of multiple helices of dinuclear alkynylplatinum(II) complex with luminescence enhancement behavior. *Chem. Sci.* **2013**, *4*, 4228–4234. [[CrossRef](#)]
58. Liu, S.; Sun, H.; Ma, Y.; Ye, S.; Liu, X.; Zhou, X.; Mou, X.; Wang, L.; Zhao, Q.; Huang, W. Rational design of metallophosphors with tunable aggregation-induced phosphorescent emission and their promising applications in time-resolved luminescence assay and targeted luminescence imaging of cancer cells. *J. Mater. Chem.* **2012**, *22*, 22167–22173. [[CrossRef](#)]
59. Schmidbaur, H. Ludwig Mond Lecture. High-carat gold compounds. *Chem. Soc. Rev.* **1995**, *24*, 391–400. [[CrossRef](#)]
60. King, C.; Khan, M.N.I.; Staples, R.J.; Fackler, J.P. Luminescent Mononuclear Gold(I) Phosphines. *Inorg. Chem.* **1992**, *31*, 3236–3238. [[CrossRef](#)]
61. Yang, Y.; Chen, J.S.; Liu, J.Y.; Zhao, G.J.; Liu, L.; Han, K.L.; Cook, T.R.; Stang, P.J. Photophysical Properties of a Post-Self-Assembly Host/Guest Coordination Cage: Visible Light Driven Core-to-Cage Charge Transfer. *J. Phys. Chem. Lett.* **2015**, *6*, 1942–1947. [[CrossRef](#)] [[PubMed](#)]
62. Wegeberg, C.; Wenger, O.S. Luminescent First-Row Transition Metal Complexes. *JACS Au* **2021**, *1*, 1860–1876. [[CrossRef](#)] [[PubMed](#)]

Disclaimer/Publisher's Note: The statements, opinions and data contained in all publications are solely those of the individual author(s) and contributor(s) and not of MDPI and/or the editor(s). MDPI and/or the editor(s) disclaim responsibility for any injury to people or property resulting from any ideas, methods, instructions or products referred to in the content.